Computer Assisted Mechanics and Engineering Sciences, 13: 269–304, 2006.

Simulation of the MARA 10 test representing a core disruptive accident

Marie-France Robbe
CEA Saclay, bât 118, 91191 Gif sur Yvette cedex, France
e-mail: marie-france.robbe@cea.fr

Michel Lepareux
CEA Saclay, SEMT-DYN, 91191 Gif sur Yvette cedex, France

Folco Casadei
JRC Ispra, IPSC, T.P. 480, I-21020 Ispra, Italy

(Received November 29, 2004)

In the case of a Hypothetical Core Disruptive Accident in a Liquid Metal Fast Breeder Reactor, the core of the nuclear reactor is assumed to have partially melted, and the interaction between molten fuel and liquid sodium creates a high-pressure gas bubble in the core. The violent expansion of this bubble loads and deforms the reactor vessel and the internal structures, thus endangering the safety of the nuclear plant.

The MARA 10 experimental test simulates a HCDA in a 1/30-scale mock-up schematising simply a reactor block. The vessel is filled with water, topped with an air blanket. The test is fired using an explosive charge. This paper presents the numerical models implemented in the EUROPLEXUS code, and a numerical simulation of the test. The evolution of the fluid flows and the deformations of structures are analysed in detail to understand the progress of the explosive phenomenon.

Keywords: accident, simulation, dynamic, mechanics, nuclear, reactor, explosion

1. Introduction

To ensure a high safety level in French nuclear power plants, safety authorities require plant designers to take into consideration several cases of hypothetical severe accidents which the plant must be able to withstand. The aim is to guarantee that even a core-melt accident would not require any stringent countermeasures such as evacuation or relocation of the population beyond the immediate vicinity of the plant.

For the Liquid Metal Fast Breeder Reactors (LMFBR), one of the accidents envisaged is a Hypothetical Core Disruptive Accident (HCDA). The scenario supposes that the core of the reactor has partially melted. The contact of the molten fuel with the liquid sodium used to cool the reactor core, causes a very quick vaporisation of sodium. A high-pressure gas bubble forms in the core centre. The explosive expansion of this bubble leads to overloading the reactor vessel and its internal structures.

During the 1970s and 1980s, the reactor integrity was studied using several computer codes validated by experimental data. Experimental programmes, undertaken by different countries, consisted in simplified small-scale mock-ups representing reactors: APRICOT [64], FTR and CBR detail scale models [7], STROVA [34], COVA [2, 31, 32, 33, 63], WINCON [57] and MARA.

Based on small-scale models of the Superphenix reactor, the French programme MARA involved eleven tests:

- MARA 1 and 2 considered a vessel partially filled with water and topped with a rigid roof [1],
- MARA 4 represented, in addition, the main core support structures [59],
- MARA 8 and 9 used a flexible roof and a flexible vessel [26],
- MARA 10 included a simplified representation of the structures surrounding the core [40],
- MARS [25] was a 1/20-scale mock-up including all the significant internal components.

A lot of computer codes were used to simulate Core Disruptive Accidents. In the United States, not less than seven codes were available: PISCES 2 DELK [21], REXCO [17], MICE, ICECO, ICEPEL, STRAW and SADCAT [18]. In Europe, several 2D axisymmetrical codes were used: SURBOUM [61], SEURBNUK [8] for compressible fluids coupled to EURDYN for structures [58, 60], and ASTARTE [20].

In France, two 2D axisymmetrical computer codes specialised in CDA computations were developed by the CEA-Cadarache: CASSIOPEE [28] and SIRIUS [4]. The SIRIUS code [1, 22] was validated by the MARA programme [5, 41].

At the beginning of the 1990s, the French teams stopped using the SIRIUS code and preferred to add a specific CDA sodium-bubble-argon tri-component constitutive law [37] to the general fast-dynamics CASTEM-PLEXUS code. The CDA constitutive law was validated [11] by the CONT benchmark [3].

In order to demonstrate the capability of CASTEM-PLEXUS to predict the behaviour of real reactors [10, 38], axisymmetrical computations of the MARA 8 and MARA 10 tests were confronted with the experimental results. Globally, the computations were in rather good agreement with the tests [9].

The merging of CASTEM-PLEXUS with the PLEXIS-3C code extended the capacities of both codes. The newly created EUROPLEXUS code benefited from new methods to treat fluid-structure coupling and another comparison was undertaken for the MARA 8 [47, 51] and MARA 10 mock-ups [52]. These simulations presented results in closer agreement with the tests. However, some discrepancies persisted.

To conclude the MARA 10 test, another simulation with a finer mesh and an improvement of the fluid-structure coupling was undertaken. Owing to the enlargement of the computer capacities, it was possible to carry out the simulation for a longer period of physical time. After a presentation of the EUROPLEXUS code, this paper focuses on the MARA 10 mock-up, the numerical model, and the analysis of the numerical results.

2. Description of the models implemented in the europlexus code

2.1. The EUROPLEXUS computer code

EUROPLEXUS is a general computer code [6, 16, 19, 30, 45], co-developed by CEA-Saclay and JRC-Ispra, for the analysis of fast transient phenomena. EUROPLEXUS results from the merging of the CASTEM-PLEXUS and PLEXIS-3C codes. It can perform 1D, 2D or 3D structure calculations as required.

The main fields dealt with are impacts, explosions [46, 48, 49, 53], pipe circuits [35, 54], blowdowns [43, 44, 50, 55], hydrodynamics [62] and robots [39].

EUROPLEXUS is mainly based on the Finite Element Method, but it also contains finite volumes and spectral elements. Time integration is explicit and realised with a Newmark algorithm. The formulation can be Lagrangian, Eulerian or Arbitrary Lagrange Euler (ALE). The code can take into account various non-linearities related to materials or geometry.

The algorithm of EUROPLEXUS with the ALE description is described below. The Lagrangian and Eulerian descriptions can be deduced easily from the ALE equations:

- the velocity of the grid is $\mathbf{w} = \mathbf{0}$ for the Eulerian description,
- the velocity of the grid is equal to that of the material particles for the Lagrangian description: $\mathbf{w} = \mathbf{v}$.

At time $t^{(n)}$, are known the coordinates $\mathbf{y}$ and velocities $\mathbf{w}$ of the grid, the velocities $\mathbf{v}$ and accelerations $\boldsymbol{\gamma}$ of the material particles, the density ρ, the mass M, and the internal energy I.

The geometry, displacements $\mathbf{q}$ and intermediate velocities of the material points and the grid are updated [36].

$$\mathbf{w}^{(n+1/2)} = f\left(\mathbf{y}^{(n)}, \mathbf{w}^{(n-1/2)}\right) \tag{1}$$

is provided by the algorithm of automatic remeshing [27],

$$\mathbf{y}^{(n+1)} = \mathbf{y}^{(n)} + \left(t^{(n+1)} - t^{(n)}\right) \mathbf{w}^{(n+1/2)}, \tag{2}$$

$$\mathbf{q}^{(n+1)} = \mathbf{y}^{(n+1)} - \mathbf{y}^{(n)}, \tag{3}$$

$$\mathbf{v}^{(n+1/2)} = \mathbf{v}^{(n)} + \frac{1}{2}\left(t^{(n+1)} - t^{(n)}\right) \boldsymbol{\gamma}^{(n)}. \tag{4}$$

The mass conservation is ensured by balancing the flows crossing the mesh boundary of the element during the time step [24]:

$$M_e^{(n+1)} = M_e^{(n)} - \int_{t^{(n)}}^{t^{(n+1)}} \oint_A \rho_e^{(n)} \left(\mathbf{w}^{(n+1/2)} - \mathbf{v}^{(n+1/2)}\right) .\mathbf{n}\, \mathrm{d}A\, \mathrm{d}t + \int_{t^{(n)}}^{t^{(n+1)}} \int_V M_{\mathrm{ext}}\, \mathrm{d}V\, \mathrm{d}t, \tag{5}$$

where $\mathbf{n}$, M_{ext}, A and V are the normal vector, an external source of mass, the bounding surface and the volume of the element, respectively.

Use is made of the change of element volume given by:

$$V_e^{(n+1)} = V_e^{(n)} + \int_{t^{(n)}}^{t^{(n+1)}} \oint_A \mathbf{w}^{(n+1/2)} .\mathbf{n}\, \mathrm{d}A\, \mathrm{d}t \tag{6}$$

to update the element density via

$$\rho_e^{(n+1)} = M_e^{(n+1)} / V_e^{(n+1)}. \tag{7}$$

The strain increment is given by:

$$\Delta \overline{\overline{\varepsilon}}_e^{(n+1)} = \overline{\overline{B}}_e^{(n+1)} \mathbf{q}^{(n+1)}, \tag{8}$$

where $\overline{\overline{B}}$ is the matrix of the spatial derivatives of the shape functions.

The new pressure and stresses are obtained in two steps: first the stresses at time $t^{(n)}$ are computed again for the new geometry, then the material constitutive law provides the stress increment between times $t^{(n)}$ and $t^{(n+1)}$.

$$\overline{\overline{\sigma}}_e^{(n+1)} = \overline{\overline{\pi}}_e^{(n)}(\mathbf{y}^{(n+1)}) + \Delta \overline{\overline{\pi}}_e^{(n+1)}(\mathbf{y}^{(n+1)}) = \overline{\overline{\pi}}_e^{(n)}(\mathbf{y}^{(n+1)}) + \overline{\overline{D}}_e \Delta \overline{\overline{\varepsilon}}_e^{(n+1)}, \tag{9}$$

where $\overline{\overline{D}}$, $\overline{\overline{\sigma}}$ and $\overline{\overline{\pi}}$ are the tensor characterizing the behaviour of the material, the Cauchy's tensor of stresses, and the Piola–Kirchoff's tensor of stresses, respectively.

The internal energy I and the specific internal energy i are updated:

$$I_e^{(n+1)} = I_e^{(n)} + \int_{t^{(n)}}^{t^{(n+1)}} \oint_A \rho_e^{(n+1)} i_e^{(n)} \left(\mathbf{w}^{(n+1/2)} - \mathbf{v}^{(n+1/2)}\right).\mathbf{n}\, \mathrm{d}A\, \mathrm{d}t + \int_{t^{(n)}}^{t^{(n+1)}} \oint_A \left(\overline{\overline{\sigma}}_e^{(n+1)}.\mathbf{n}\right).\mathbf{v}^{(n+1/2)}\, \mathrm{d}A\, \mathrm{d}t, \tag{10}$$

$$i_e^{(n+1)} = I_e^{(n+1)}/M_e^{(n+1)}. \tag{11}$$

The code computes the internal force $\mathbf{F}_{\text{int}}$, the transport force $\mathbf{F}_{\text{trans}}$, the connection force $\mathbf{F}_c$ and the external force $\mathbf{F}_{\text{ext}}$:

$$\mathbf{F}_{\text{int}}^{(n+1)} = \int_V \overline{\overline{B}}^{(n+1)^{\mathrm{T}}} \overline{\overline{\sigma}}^{(n+1)} \mathrm{d}V, \tag{12}$$

$$\mathbf{F}_{\text{trans}}^{(n+1)} = \oint_A \rho^{(n+1)} \mathbf{v}^{(n+1/2)} \left(\mathbf{w}^{(n+1/2)} - \mathbf{v}^{(n+1/2)}\right).\mathbf{n}\, \mathrm{d}A, \tag{13}$$

$$\mathbf{F}_c^{(n+1)} = \int_V \overline{\overline{C}}^{\mathrm{T}} \zeta^{(n+1)} \mathrm{d}V, \tag{14}$$

where $\overline{\overline{C}}$ and ζ are the symmetric matrix of connections and boundary conditions, and the vector of Lagrange multipliers, respectively.

Then the code assembles the matrices for the entire geometry, and solves the weak formulation of the momentum equation:

$$\overline{\overline{M}}^{(n+1)}.\boldsymbol{\gamma}^{(n+1)} = \mathbf{F}_{\text{trans}}^{(n+1)} - \mathbf{F}_{\text{int}}^{(n+1)} + \mathbf{F}_c^{(n+1)} + \mathbf{F}_{\text{ext}}^{(n+1)} \tag{15}$$

and computes the new velocities of the material points:

$$\mathbf{v}^{(n+1)} = \mathbf{v}^{(n)} + \frac{t^{(n+1)} - t^{(n)}}{2} \left(\boldsymbol{\gamma}^{(n)} + \boldsymbol{\gamma}^{(n+1)}\right). \tag{16}$$

The code calculates the kinetic energy E_{kin}, and the external energy E_{ext} (energy brought to the system from outside).

$$E_{\text{kin}}^{(n+1)} = \oint_A \rho^{(n+1)} \frac{1}{2} \parallel \mathbf{v}^{(n+1)} \parallel^2 \left(\mathbf{w}^{(n+1/2)} - \mathbf{v}^{(n+1)}\right).\mathbf{n}\, \mathrm{d}A. \tag{17}$$

Finally the code checks the energy balance: the energy received from outside must be balanced by the energy stored into the system and that used to move it. As the mechanical equilibrium of the entire system can require some time steps, a small gap can exist during some 10^{-8} s.

$$E_{\text{ext}}^{(n+1)} \simeq I^{(n+1)} + E_{\text{kin}}^{(n+1)}. \tag{18}$$

2.2. The CDA constitutive law

A Core Disruptive Accident (CDA) in a Liquid Metal Fast Breeder Reactor (LMFBR) involves three fluid components: liquid sodium, argon and a gas bubble. A specific CDA constitutive law was implemented in the EUROPLEXUS code in order to be able to represent very precisely this kind of explosion. As this law assumes that phenomena of thermal transfers and phase slide are too slow to happen during the explosion, the code does not use the energy equation for the resolution of CDA problems.

To simplify the numerical model, the sodium-argon-bubble mixture is supposed to be homogeneous in each mesh. The CDA constitutive law considers that the three components can mix during

the bubble expansion and sodium can cavitate. Therefore it includes four fluid fields: liquid sodium, sodium vapour at saturation conditions, argon and bubble.

In the Finite Element Model, the nodal variables (velocity, acceleration, etc.) are identical for the three constituents of the CDA law. The elementary variables (pressure, density, etc.) depend on several parameters: the partial variables of each constituent, the presence fraction x of constituents, etc. Quantities related to a specific constituent (a for argon, b for bubble, s for sodium and v for sodium vapour) are indicated with a subscript. Quantities without a subscript are related to the homogeneous mixture and the index g is related to the gas mixture.

The pressure of the gas mixture p_g is the sum of partial pressures:

$$p_g^{(n+1)} = p_a^{(n+1)} + p_b^{(n+1)} + p_v^{(n+1)}. \tag{19}$$

The density of the mixture is given by:

$$\rho = \rho_a\, x_a + \rho_b\, x_b + \rho_s\, x_s + \rho_v\, x_v. \tag{20}$$

The void fraction α is obtained from the ratios between the relative density ϕ of a component (density related to the total volume of the mesh) and the absolute density of the component:

$$\alpha = \frac{\phi_a}{\rho_a} = \frac{\phi_b}{\rho_b} = \frac{\phi_v}{\rho_v} = \frac{\phi_g}{\rho_g} = 1 - \frac{\phi_s}{\rho_s}. \tag{21}$$

Each component is described by a specific constitutive law, and the presence of the other components is assumed not to affect the law of each one [38]. The four fluid fields are described as perfect gases or perfect fluids, thus there are supposed inviscid, and an eventual turbulence is not taken into account.

The fluid fields are characterized by the following laws:

Argon: Perfect gas with an adiabatic behaviour

$$p_a^{(n+1)} = p_a^{(n)} \left(\frac{\rho_a^{(n+1)}}{\rho_a^{(n)}} \right)^{\lambda_a}, \tag{22}$$

where $\lambda_a = c_p/c_v$ is the heat capacity ratio.

Bubble: Perfect gas described by a polytropic law

$$p_b^{(n+1)} = p_b^{(n)} \left(\frac{\rho_b^{(n+1)}}{\rho_b^{(n)}} \right)^{\eta_b}. \tag{23}$$

The exponent η_b can have any positive value. For instance, $\eta_b = 1$ for an isothermal law or $\eta_b = \lambda_b$ for an adiabatic law.

Liquid sodium: Perfect and isothermal fluid

$$p_s^{(n+1)} = p_g^{(n+1)} = p_s^{(n)} + C_s^2 \left(\rho_s^{(n+1)} - \rho_s^{(n)} \right) \tag{24}$$

with C_s the sound velocity in sodium.

Sodium vapour: The diphasic sodium is at saturation conditions.
If $p_s^{(n+1)} > p_{\text{sat}}$, then the presence fraction of the sodium vapour x_v is negligible.
If pressure decreases, the sodium pressure can reach the saturation pressure; the vaporisation is supposed to be instantaneous. The sodium vapour is an isothermal perfect gas whose pressure is constant and only depends on the initial temperature $T^{(0)}$:

$$p_v^{(n+1)} = p_{\text{saturation}} \left(T^{(0)} \right). \tag{25}$$

The thermal equilibrium requires a very long time, compared to the duration of the explosive phenomenon (the explosion is considered to be ended after 20 ms from the mechanical point of view). Thus saturation data depending on the initial temperature are sufficient, and the heat of vaporization is not considered.

EUROPLEXUS computes the average density from the mass conservation. Then the pressure and composition of the mixture are obtained by successive iterations. The iterative process computes:

1. The sodium density from (24) by estimating approximately $p_s^{(n+1)}$ at the beginning of the time step,
2. The void fraction and then the argon and bubble densities from (21),
3. The argon pressure from (22),
4. The bubble pressure from (23),
5. The mixture pressure from (19).

2.3. Fluid-structure interaction

EUROPLEXUS can represent problems involving fluids and/or structures with a possibility of coupling. Three principal methods were successively implemented to deal with the fluid-structure interaction: the FS2D method is based on the definition of coupling elements, whereas the FSA and UP methods just require the definition of fluid nodes located along the solid interface.

2.3.1. FS2D method

A special "fluid-structure coupling element" has to be defined by the user. In 2D, the coupling element is a flattened rectangle: two nodes of the long side lay on the fluid side while the two facing nodes lay on the solid side. A connection condition of type "no variation of volume" is considered:

$$\overline{\overline{C}}\,\mathrm{d}\mathbf{q} = \mathbf{0} \tag{26}$$

so that the fluid node has the same displacement as the facing solid node. In the connection force, the Lagrange multipliers are equal to pressure [30]:

$$\mathbf{F}_c^{(n+1)} = \int_V \overline{\overline{C}}^{\mathrm{T}}\, p\,\mathbf{I}\,\mathrm{d}V, \tag{27}$$

where $\mathbf{I}$ is the unit vector.

2.3.2. FSA method

The treatment of fluid-structure coupling with permanent contact is based on a method of Lagrange multipliers, as for boundary conditions. The fluid is supposed to be compressible and inviscid. A permanent contact is defined as a situation whereby a structure is in contact with a fluid during the entire time interval of interest, and the fluid is always of the same type and nature, what excludes the vicinity of free surfaces and fluid/fluid interfaces without mixing.

With the Fluid-Structure ALE method (FSA), two sets of nodes are defined along fluid-structure interfaces: the one on the fluid side and the other one on the solid side. They must coincide two by two with each other. The solid nodes are treated as Lagrangian nodes, while the fluid ones are ALE. The motion of the fluid mesh is automatically prescribed by EUROPLEXUS in such a way that the fluid mesh is permanently aligned with the structural mesh along the interface.

The study of the behaviour of fluid and structure can be decoupled, provided the interaction force is known at each node of the interface and at every time. To find the interaction force, a compatibility condition is imposed: at every instant, the velocity of the fluid f along the normal to the interface must be equal to the velocity of the structure s along the same direction, and fluid must permanently stay in contact with the (moving) structural wall [14].

$$\mathbf{v}_f.\mathbf{n} = \mathbf{v}_s.\mathbf{n}, \tag{28}$$

$$\mathbf{w}_f = \mathbf{w}_s. \tag{29}$$

This condition ensures that the fluid and solid domains do not detach or overlap during the motion. The motion of the fluid and the structure are coupled in the direction normal to the interface, while each component is free to move on its own in the tangential direction.

EUROPLEXUS writes down automatically the appropriate compatibility conditions for each interaction pattern, introduces the resulting equations in the global matrix of connections, assembles them together with other kinds of boundary conditions, and finally solves the problem numerically.

To determine the local normal to a discrete interface, only the fluid domain is considered in the vicinity of the node for the FSA method. The direction of the normal is determined by imposing that the net velocity flux across the discrete interface in all the fluid element faces in contact with the structure that contains the fluid node must vanish, in order to avoid artificial gains or losses of fluid.

$$\mathbf{n} = \frac{\sum_{k=1}^{\text{faces}} \mathbf{n}_k}{\| \sum_{k=1}^{\text{faces}} \mathbf{n}_k \|}. \tag{30}$$

In presence of structural edges without a topological thickness (thin shells) and completely submerged by fluid, the method leads to an undefined zero-length normal. The algorithm must be modified: the couples of mutually opposite faces in the influence domain are detected and one of these double faces is eliminated for each couple [13].

Among the potential solutions for the normal at the edge [12], the model chosen consists in taking a normal perpendicular to the shell. The drawback of this solution lays in a spurious fluid flow when fluid turns round the edge of the shell: as the fluid velocity at the edge is unique, fluid flows in the same direction along both sides of the edge.

In case of curved non-planar surfaces, the FSA algorithm may lead to the appearance of spurious velocities, due to a small but non-negligible error in the evaluation of the discrete normal (small unbalance between the internal forces generated by the fluid pressure and external forces represented by the reactions produced by the rigid walls).

2.3.3. UP method

To overcome this problem of spurious velocities, a different approach was developed. The Uniform Pressure method [15] is based on the same concept of Lagrange multipliers as the FSA method. The difference comes from the determination of the normal, based on equilibrium rather than geometric considerations. The UP method relies upon the observation that the direction of the discrete normal is exactly prescribed by the resultant of the internal forces due to an arbitrary uniform pressure in the entire fluid domain.

A fictitious internal force $\mathbf{F}_p$ generated by a uniform internal pressure ($p \simeq 1$) is introduced in all fluid elements. The contribution of each finite element to this force can be obtained simply by dividing the element "true" internal forces by pressure:

$$\mathbf{F}_p = \frac{\mathbf{F}_{\text{int}}}{p}. \tag{31}$$

After the assembly of the different element contributions, the discrete nodal normal is computed by:

$$\mathbf{n} = \frac{\mathbf{F}_p}{\| \mathbf{F}_{p\cdot} \|}. \tag{32}$$

The UP method is simple, robust and general enough to treat permanent fluid-structure interactions, but it cannot deal neither with thin shells without topological thickness and submerged by fluid, nor with sharp 3D corners.

2.4. Governing lines

The remeshing of the ALE or Lagrangian grid is usually updated automatically by the EUROPLEXUS code. In some cases (areas with violent flows or loadings, junction between two zones of very different behaviours, large deformation of structures, etc.), the automatic remeshing can lead to an excessive motion of cells, a distortion or a flattening of cells, and even hourglass. In those cases, the remeshing can be governed manually by the user.

Governing lines can be defined to impose nodes located on a line of the mesh to stay aligned. The fluid nodes of a governing line are forced to remain aligned between both extremities of the line. If the extremities of the line are fluid nodes in contact with structures, the fluid mesh adapts to the structure deformation.

Let us consider two points A and B located at the extremities of a geometric line of the mesh. Even if these nodes can have a Lagrangian, Eulerian or ALE description, they are usually Lagrangian nodes as the speed of the grid is supposed known.

Let point C be a node initially located approximately on A-B line. This point must stay aligned on the A-B line in the deformed configuration. The ratios of distances AC/CB must remain constant during the deformation of the mesh. So a condition is written between the grid speed w_C of point C and the grid speeds of points A and B which are known.

$$w_C = \nu * w_A + \mu * w_B \tag{33}$$

where ν and μ are constant coefficients. In the case of the line, these coefficients are the values of the linear shape function between A and B.

It must be noted that the particle speed $\mathbf{v}$ of fluid at point C is not affected by the remeshing condition.

3. Description of the MARA 10 mock-up

The French Liquid Metal Fast Breeder Reactors (Fig. 1) are based on an integrated design [42]: all the components of the primary circuit (core, pumps, heat exchangers, etc.) are included inside the reactor vessel. The exchanges with the secondary circuit devoted to the production of electricity are limited to some pipes crossing the roof of the reactor.

The main advantage of this design is to maintain the majority of the radioactive elements inside the reactor vessel and to limit the possible contacts between air and the radioactive sodium of the primary circuit. As sodium is easily flammable, a blanket of inert gas (argon) isolates sodium from the reactor roof.

The MARA programme was defined and carried out at the CEA-Cadarache in the 1980s in order to simulate a Core Disruptive Accident in simplified small-scale models of the Superphenix reactor block. The characteristics of the MARA mock-ups were [9]:

- A scale factor of 1/30 for all dimensions and thicknesses,
- An axisymmetrical geometry.

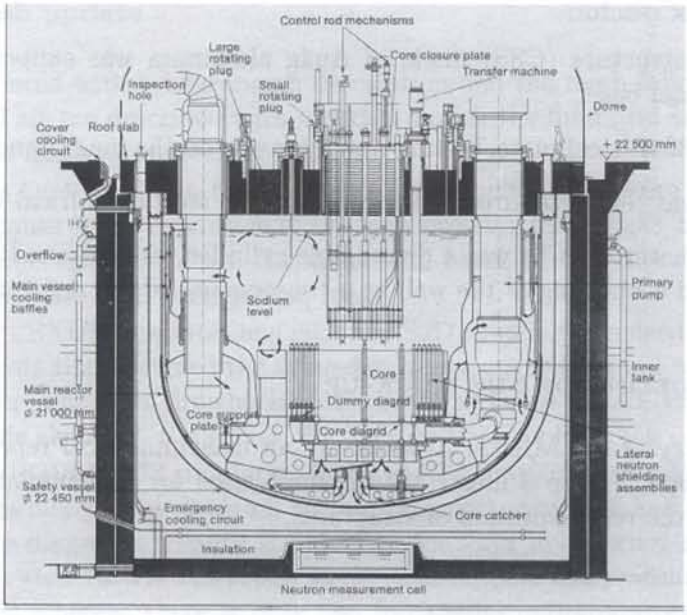

Fig. 1. The Superphenix reactor

In order to carry out tests at ambient temperature and to avoid fire problems linked to sodium handling, liquid sodium was replaced by water since both components have similar densities and viscosities. Argon was replaced by air. The bubble expansion was simulated by an explosive charge [23, 41]. In the MARA 10 test, the charge was hung up to the base of the structure above the core. The test was instrumented [40] with pressure transducers, strain gauges, high-speed cameras, and a grid drawn on the different structures.

Vessels were filled with water leaving an air gap below the roof [26]. The vessels of all the tests were identical and made of 316 steel. The vessel thickness was locally reduced between the junctions with the core support plate and the internal heat exchangers, to simulate a pinned attachment with these structures.

The external dimensions of the MARA 10 mock-up were 55 cm high and 35 cm in radius. A flexible roof A42 steel was clamped to the roof support [26]. The vessel was welded to a flange bolted to the roof support. The MARA 10 mock-up (Fig. 2) included the main internal structures

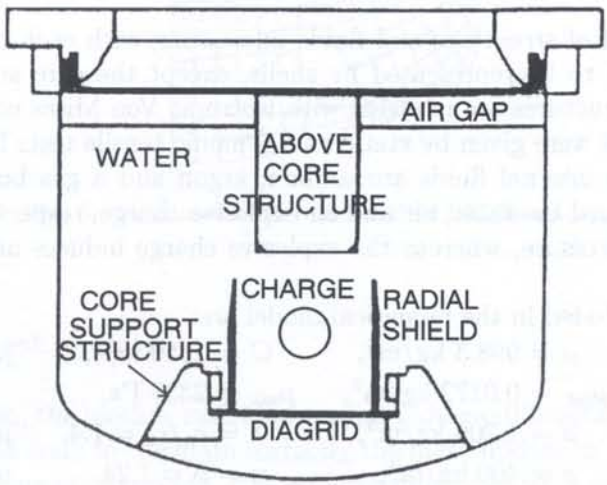

Fig. 2. The MARA 10 mock-up

[40] of the Superphenix reactor:

- The core support structure (CSS) made of Au4g aluminum was supported by a thin collar attached to the vessel base.
- The diagrid was a 304L steel plate, resting under gravity on the inner flange of the core support.
- The radial shield was represented by a deformable A316 steel cylindrical vessel,
- The above core structure (ACS) was a deformable cylinder with a base. It was completely filled with water to avoid a buckling of the wall as a consequence of the deflection of the base.

4. Numerical modeling of the mock-up

Owing to the symmetry of the MARA 10 mock-up, an axisymmetrical representation is used for the numerical simulation. Figure 3 illustrates the mesh used for the simulation of the MARA 10 test and Fig. 4 shows the representation of structures.

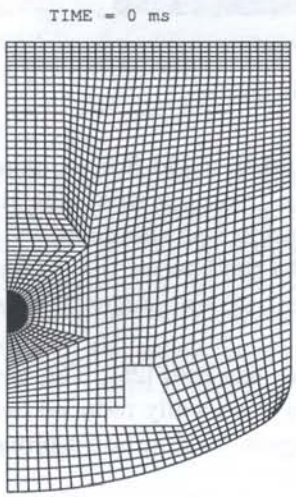

Fig. 3. Mesh used in the new EUROPLEXUS simulation

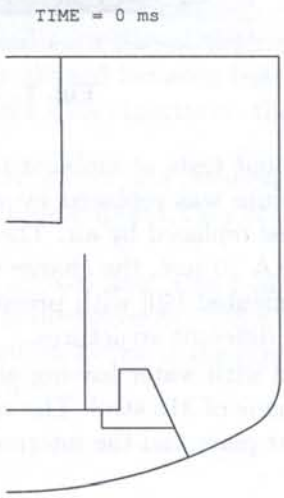

Fig. 4. Mesh of structures

4.1. Materials

The mock-up is composed of structures and fluids interacting with each other. Structures are assumed to be thin enough to be represented by shells, except the core support structure that is supposed rigid. All the structures are modeled with isotropic Von Mises constitutive laws. Experimental strain-stress curves were given by static and dynamic tensile tests for each material.

In case of a CDA, the internal fluids are sodium, argon and a gas bubble. In the MARA 10 test, these fluids are replaced by water, air and an explosive charge, respectively. Water and air are initially at atmospheric pressure, whereas the explosive charge induces an initial pressure of 165 MPa in the bubble area.

The characteristics included in the numerical model are:

- Water $\rho = 998.3$ kg/m^3, $C = 1550$ m/s, $p^{(0)} = 10^5$ Pa,
  $\rho_{\text{sat}} = 0.0172$ kg/m^3, $p_{\text{sat}} = 2337$ Pa,
- Air $\rho = 1.206$ kg/m^3, $\lambda = c_p/c_v = 1.4$, $p^{(0)} = 10^5$ Pa,
- Explosive charge $\rho = 400$ kg/m^3, $\eta = \lambda = 1.24$, $p^{(0)} = 1.646\,10^8$ Pa.

All data about water are provided by the steam tables [29]. In the current simulation, the explosive charge is supposed to be adiabatic as $\eta_b = \lambda_b$.

4.2. Automatic mesh update

Structures are represented with a Lagrangian description and the mesh follows the deformation of structures. Water and air are described with an ALE model: the fluid grid is updated according to the deformation of the neighbouring structures.

The bubble zone is kept fixed. On the one hand, if the bubble grid were ALE, the mesh would deform very much because of the expansion of the high-pressure bubble gas, and this large deformation would involve numerical difficulties. On the second hand, the fixed grid of the bubble is used as a reference to update the ALE surrounding mesh.

In the CASTEM-PLEXUS computations [9], the FS2D coupling was used: it required the definition of coupling elements that assigned the same displacements to the fluid nodes and the structure nodes facing each other. The main drawback of this coupling lay in the absence of automatic update of the ALE grid for the elements other than the ones on the coupled lines.

In the previous EUROPLEXUS simulation [52], the FSA coupling was adopted, except in a local area. As the diagrid is merely put down on the core support structure and as both structures are not rigidly linked, the diagrid extremity is linked to the CSS by a swivel contact. Consequently, there are two different structure nodes at the same location (the one pertaining to the diagrid and the other to the CSS) whereas there is only one fluid node facing the two structure ones. This configuration could not be processed by the FSA coupling some years ago.

Thanks to improvements of the FSA coupling, it is now possible to manage all the fluid-structure interfaces of the mock-up with the FSA coupling. This coupling is well adapted to complex geometries, even if it often implies a user intervention to pilot the displacements of the fluid ALE grid.

Figure 5 shows the mesh used in the previous CASTEM-PLEXUS and EUROPLEXUS simulations. The size of the cells was twice larger than in the current mesh.

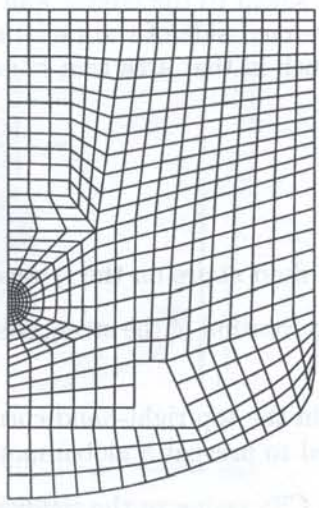

Fig. 5. Mesh used in the old EUROPLEXUS simulation

4.3. Local manual mesh update

In the current simulation, the mesh is much finer, what induces difficulties in the update of the ALE grid. In order to help the code to calculate correctly the mesh update in the areas where high-speed or high-pressure variations are expected, sixteen governing lines were defined by the user (Fig. 6). The fluid nodes of each governing line are forced to remain aligned between both extremities of the line.

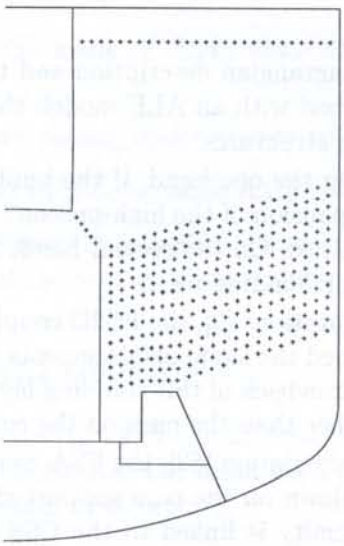

Fig. 6. Governing lines for the update of the ALE grid

One line manages the interface between the water zone and the air layer in order to prevent a flattening of the air area during the explosion due to the difference of compressibility of air and water.

A second line governs the fluid nodes between the bottom right-hand corner of the ACS base and the top of the radial shield to prevent a large deformation of the ALE grid caused by the huge fluid flows going out from the central zone. Besides, this line is used as a reference for the update of the fluid in the central zone.

A series of lines joining the radial shield to the lateral wall of the vessel helps the management of the fluid zone located on the right-hand side of the radial shield, and above the collar and the CSS, because the mesh distorts so much in that area that hourglass happens.

4.4. Boundary conditions

The boundary conditions are:

- No horizontal displacement of the fluid nodes on the symmetry axis,
- No horizontal displacement and no rotation of the structure nodes located on the symmetry axis (ACS, diagrid, vessel),
- A complete blocking of the node in the top right-hand corner at the junction of the vessel and the roof: one node must be blocked to prevent a global motion of the geometry,
- No horizontal displacement of the CSS owing to the rigidity of this massive structure,
- The vertical displacement of the diagrid extremity in contact with the CSS is equal to the one of the CSS (representation of the swivel contact).

5. Analysis of the results

The results are characterised by several variables describing the evolution of fluids and structures versus time. Figures 7 to 12 present the evolution of the hydraulic variables: pressure, volume presence fraction of gas, mass presence fraction of the bubble and air, local fluid flows, and velocity. Figures 13 to 18 show the evolution of the mechanical variables in structures: deformed shapes of the mesh and structures, radial and vertical displacements, stresses and strains.

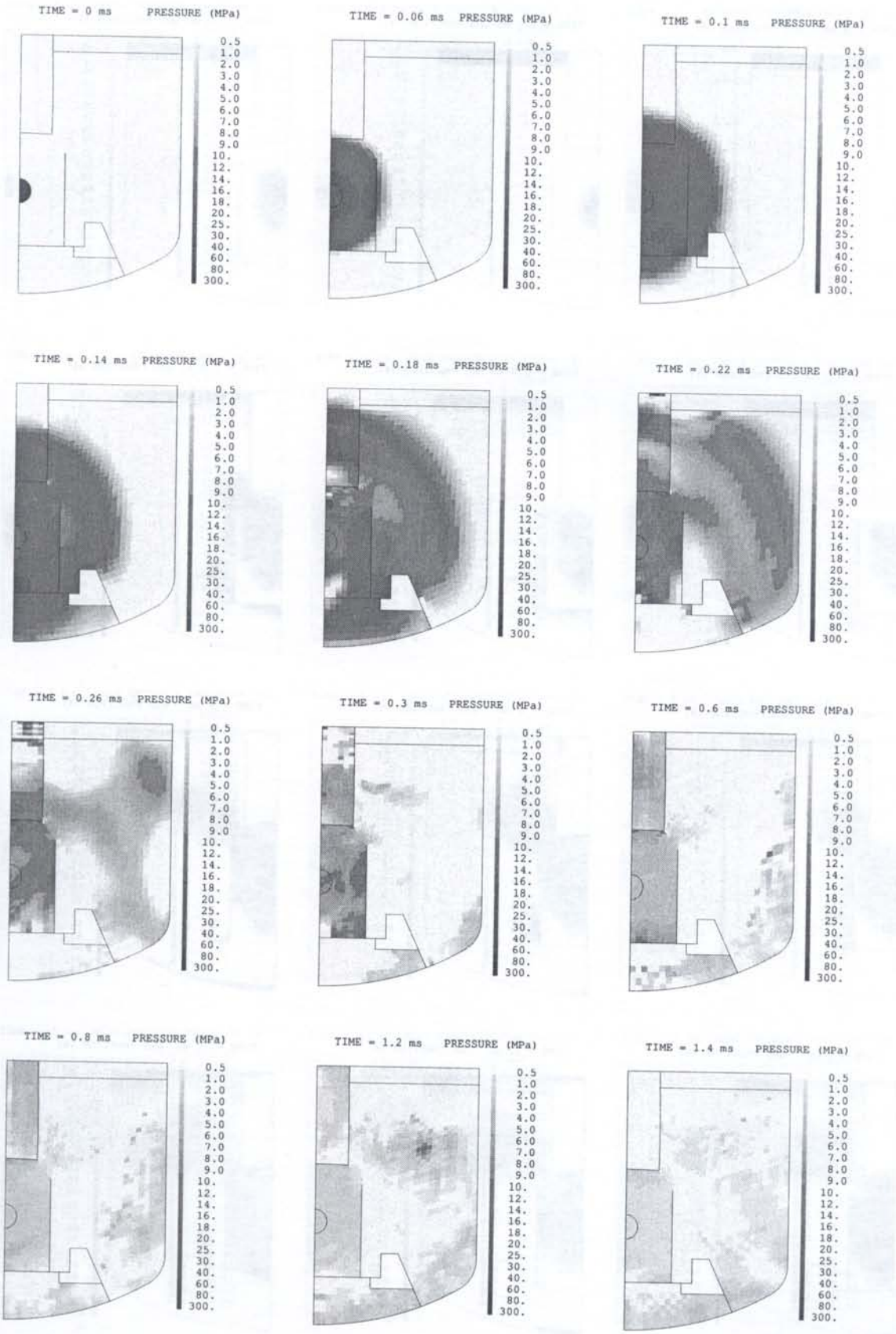

Fig. 7. Pressure

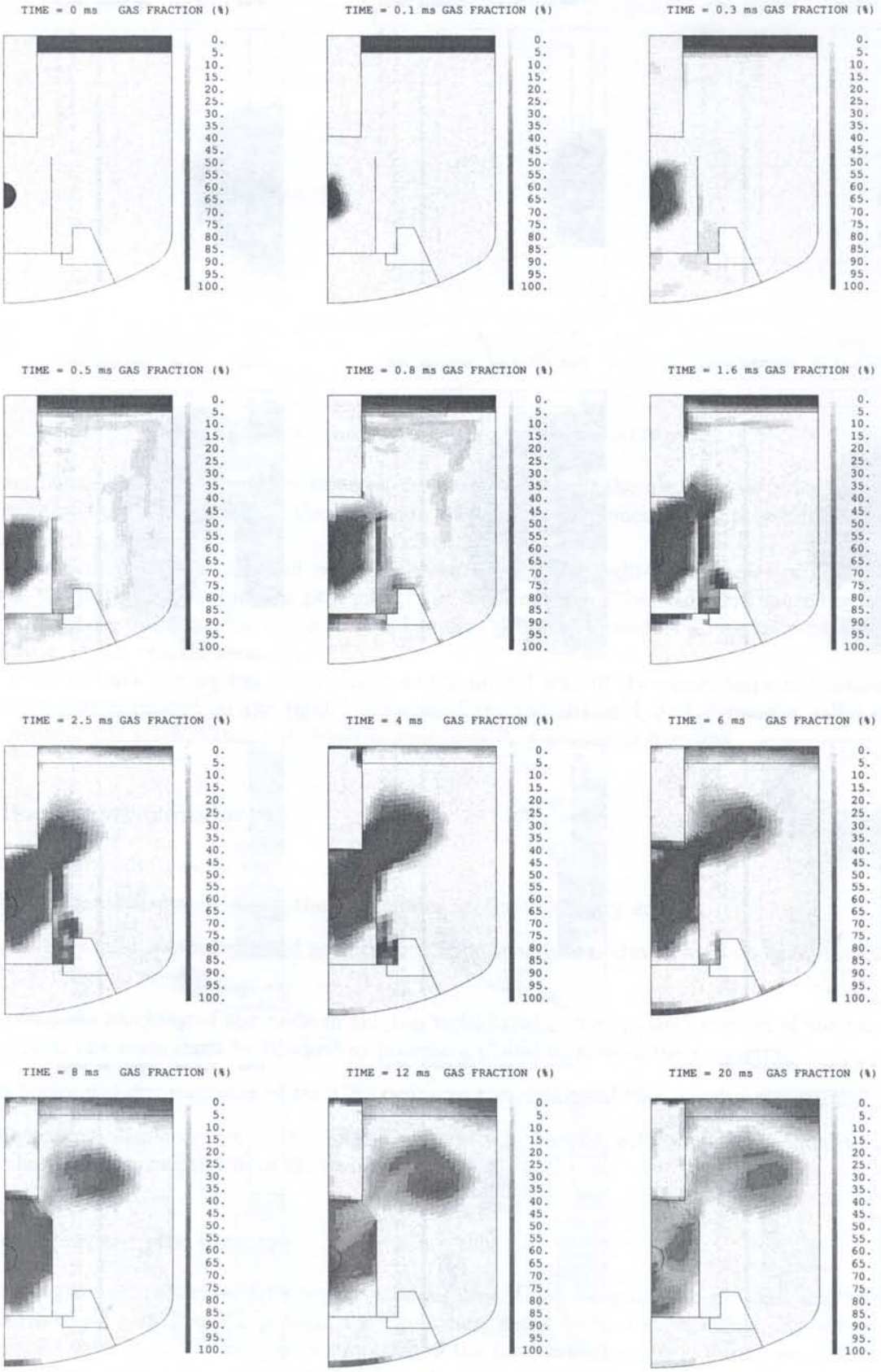

Fig. 8. Volume presence fraction of gas

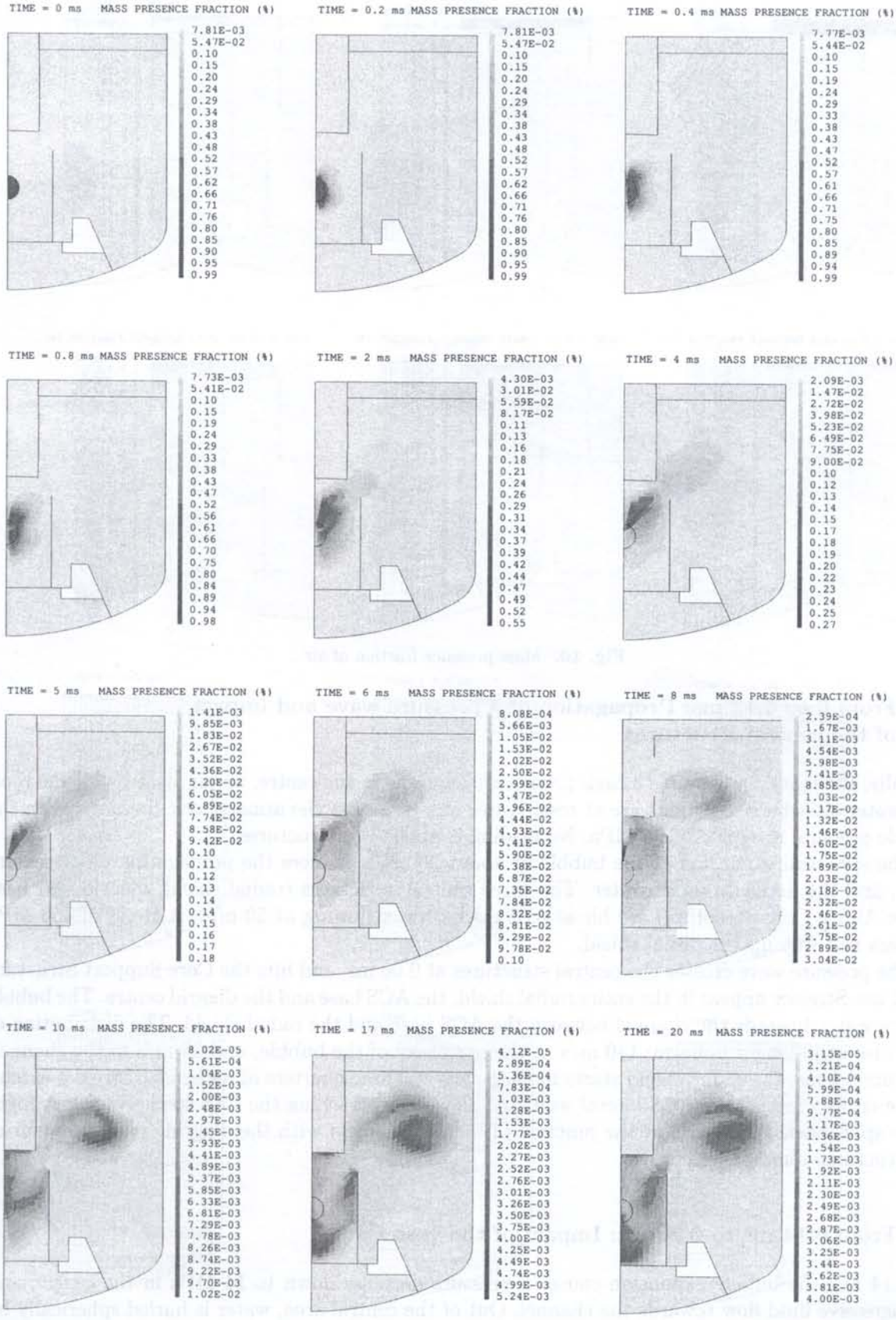

Fig. 9. Mass presence fraction of the bubble

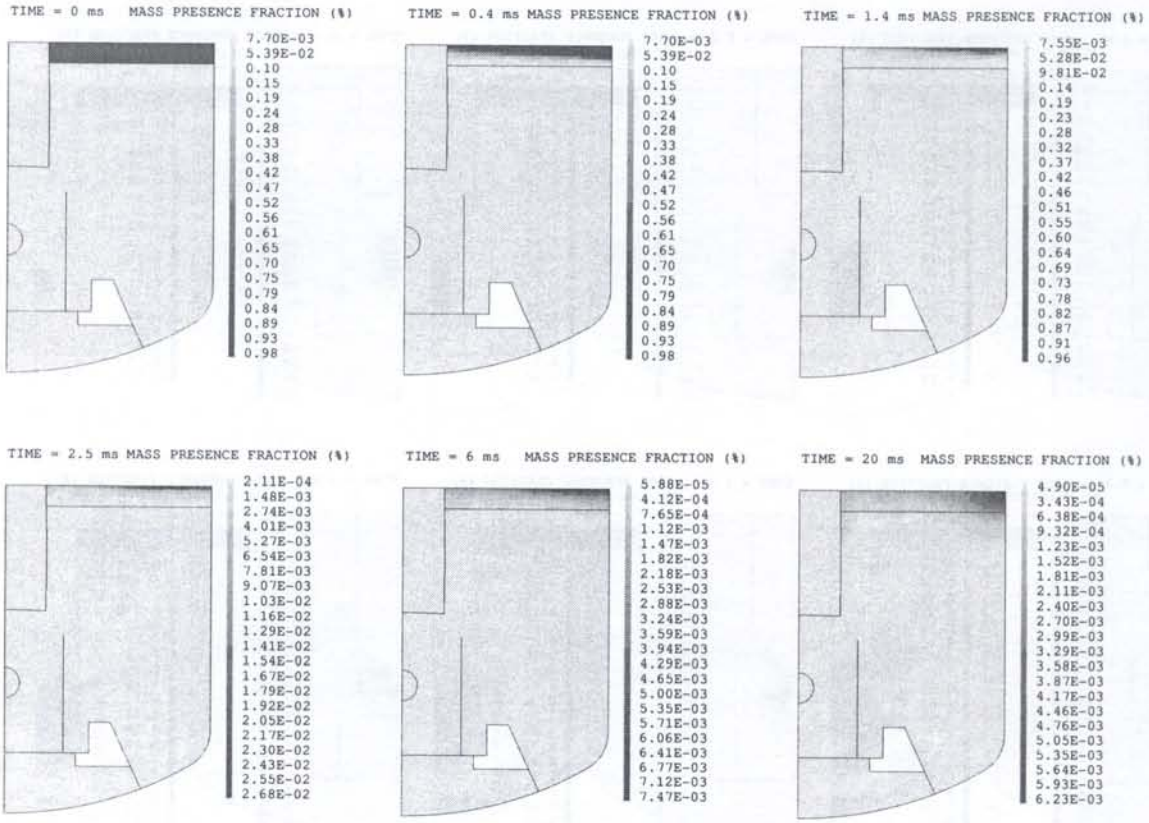

Fig. 10. Mass presence fraction of air

5.1. From 0 to 0.13 ms: Propagation of a pressure wave and impact of the central structures

Initially, the mock-up contains a high-pressure gas bubble in the centre, an air layer below the roof, and water elsewhere. All fluids are at rest. Water and air are at the atmospheric pressure while the bubble pressure is equal to 165 MPa. No loading is applied to structures.

The spherical expansion of the bubble at about 200 m/s induces the propagation of a pressure wave, and the acceleration of water. The three central structures (radial shield, diagrid and base of the Above Core Structure) are hit at 0.05 ms by water flowing at 50 m/s. A stress of 450 MPa appears half-way up the radial shield.

The pressure wave crosses the central structures at 0.06 ms, and hits the Core Support Structure at 0.1 ms. Stresses appear in the entire radial shield, the ACS base and the diagrid centre. The bubble pushes water towards the channel between the ACS base and the radial shield. The distribution of velocities is no longer uniform: 140 m/s at the periphery of the bubble, and 35 m/s in the channel.

From 0.1 ms, the radial shield starts moving away at three quarters of its height. Stresses extend to the entire diagrid, the ACS lateral wall, and the collar attaching the CSS to the vessel. A high-stress spot reaches 700 MPa at the junction of the radial shield with the diagrid. The behaviour of all structures remains elastic.

5.2. From 0.14 ms to 0.28 ms: Impact of the vessel

At 0.14 ms, the bubble expansion causes a pressure decrease down to 14 MPa in the centre, and a progressive fluid flow towards the channel. Out of the central area, water is hurled spherically by the shock wave. Water hits the vessel base, enters in the nook between the radial shield and the CSS, and turns around the CSS.

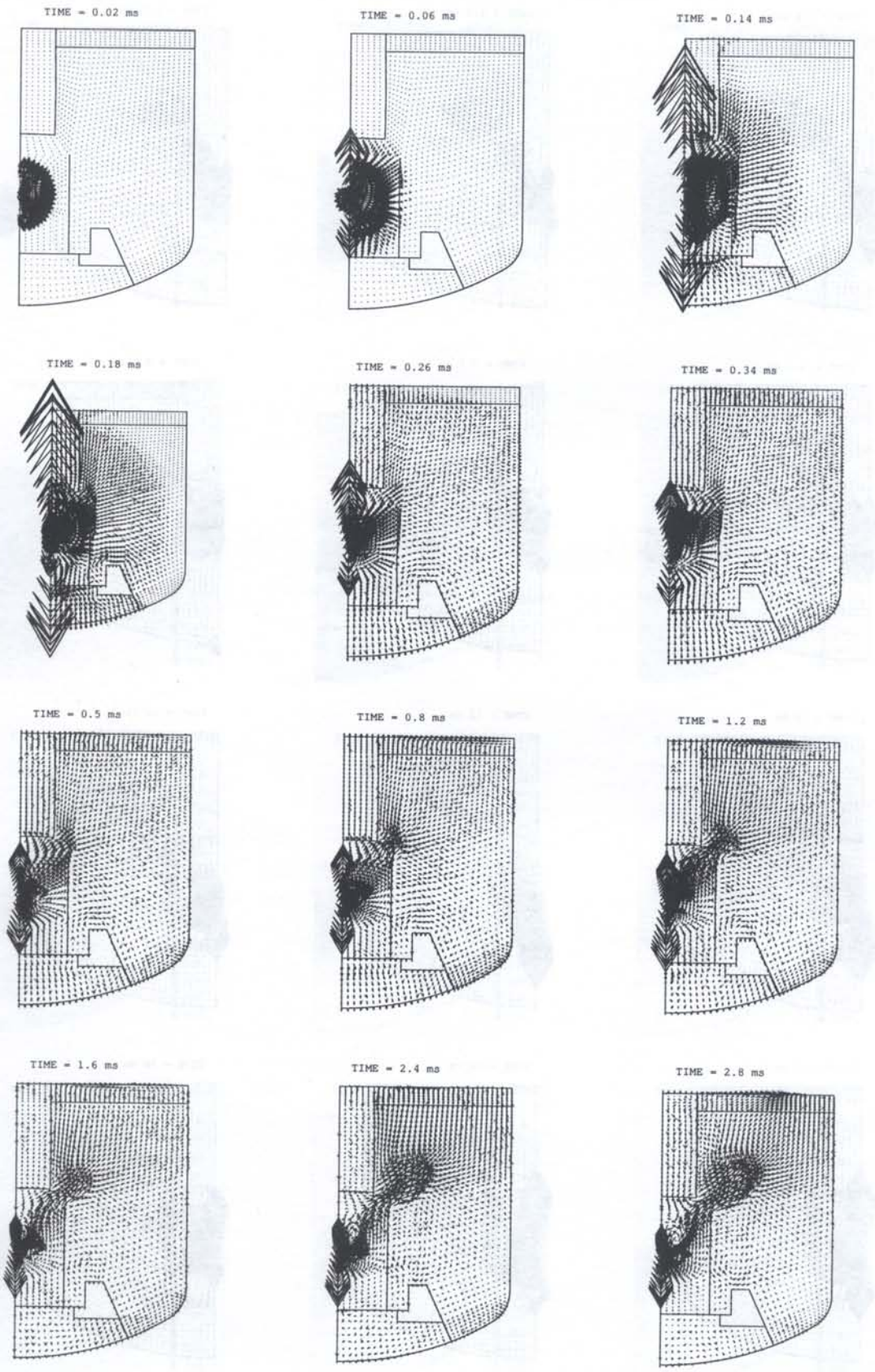
TIME = 0.02 ms
TIME = 0.06 ms
TIME = 0.14 ms
TIME = 0.18 ms
TIME = 0.26 ms
TIME = 0.34 ms
TIME = 0.5 ms
TIME = 0.8 ms
TIME = 1.2 ms
TIME = 1.6 ms
TIME = 2.4 ms
TIME = 2.8 ms

[Fig. 11a]

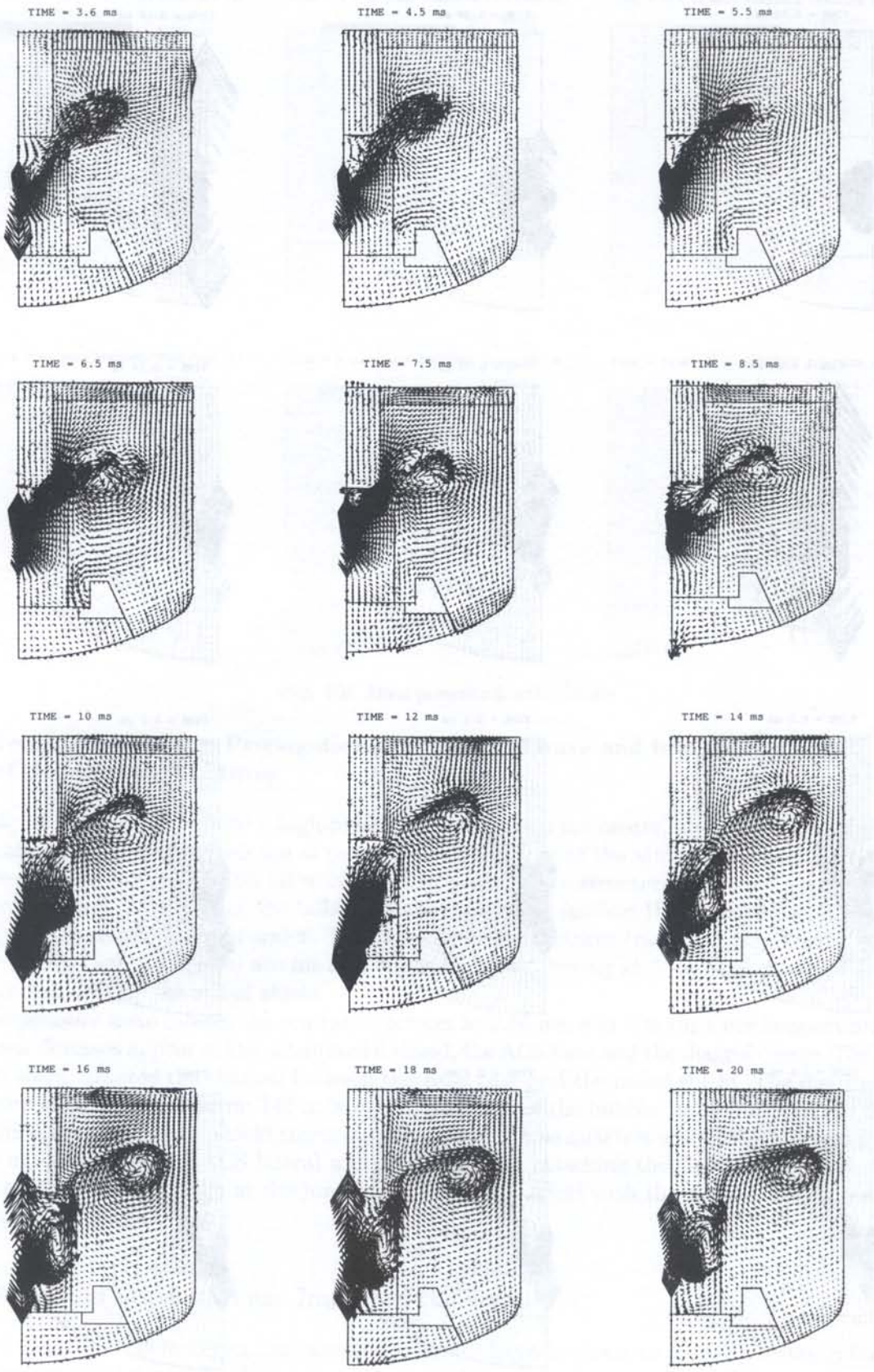

Fig. 11. Local orientation of fluid

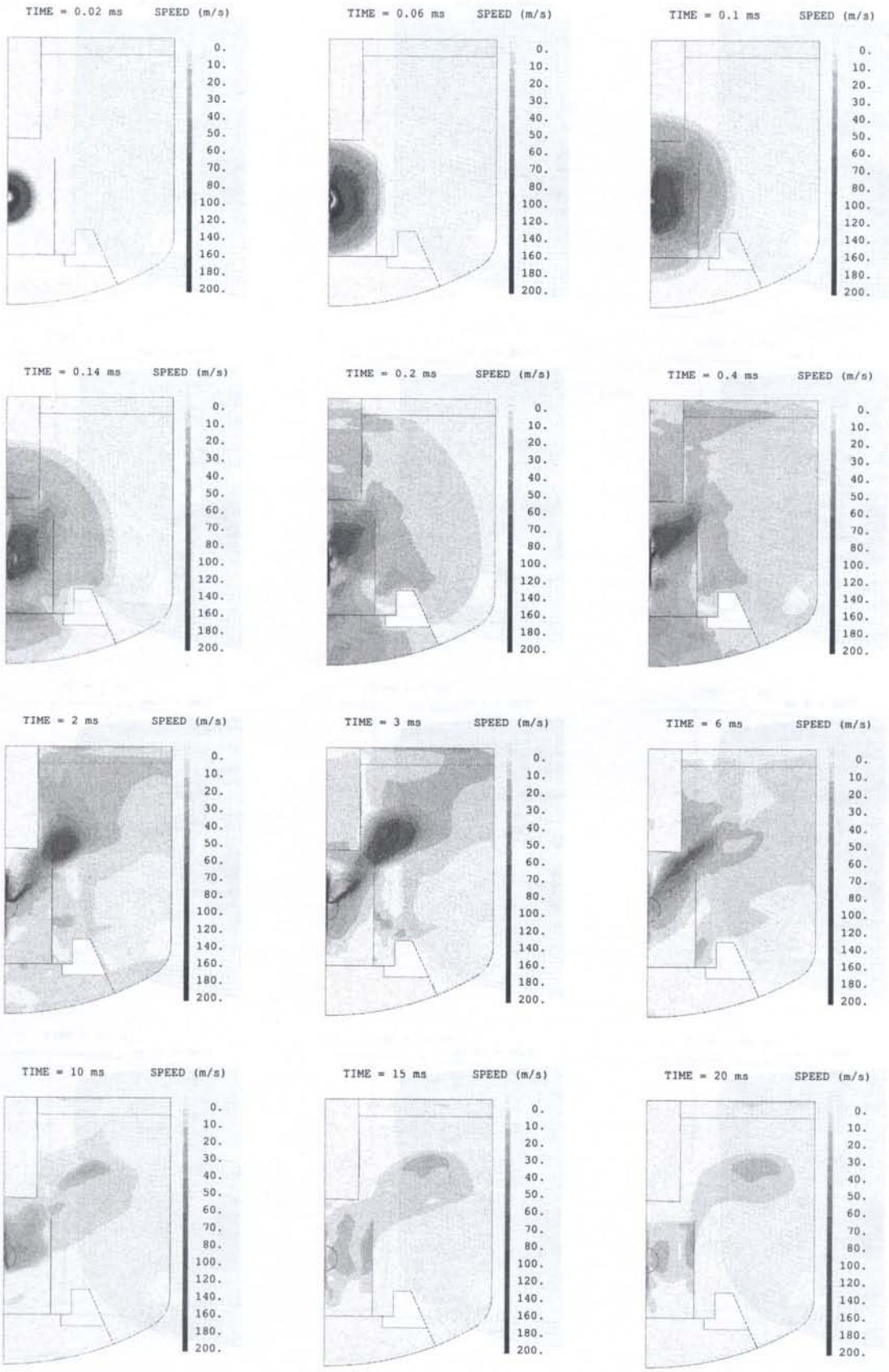

Fig. 12. Fluid speed

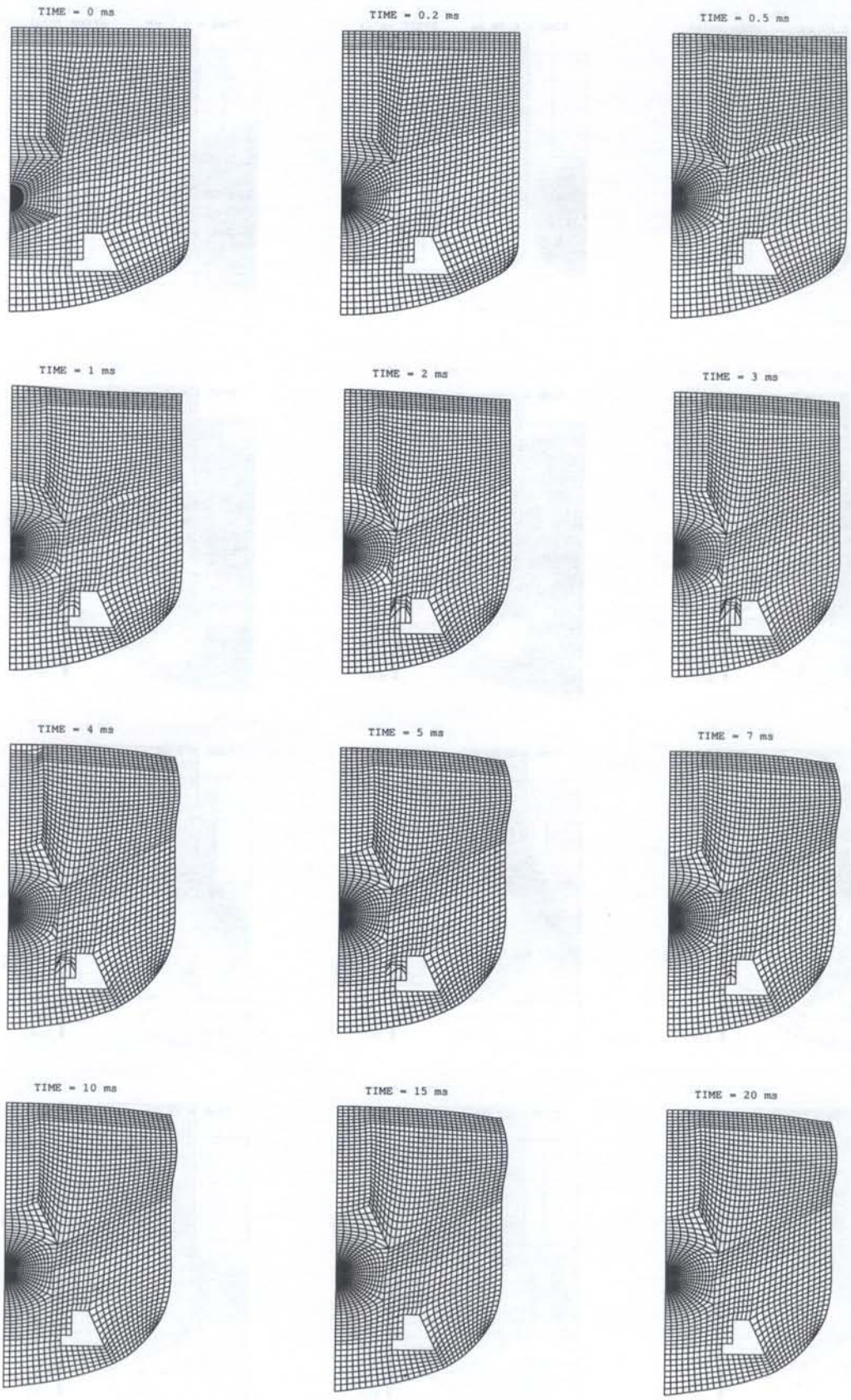

Fig. 13. Deformed shape of the mesh

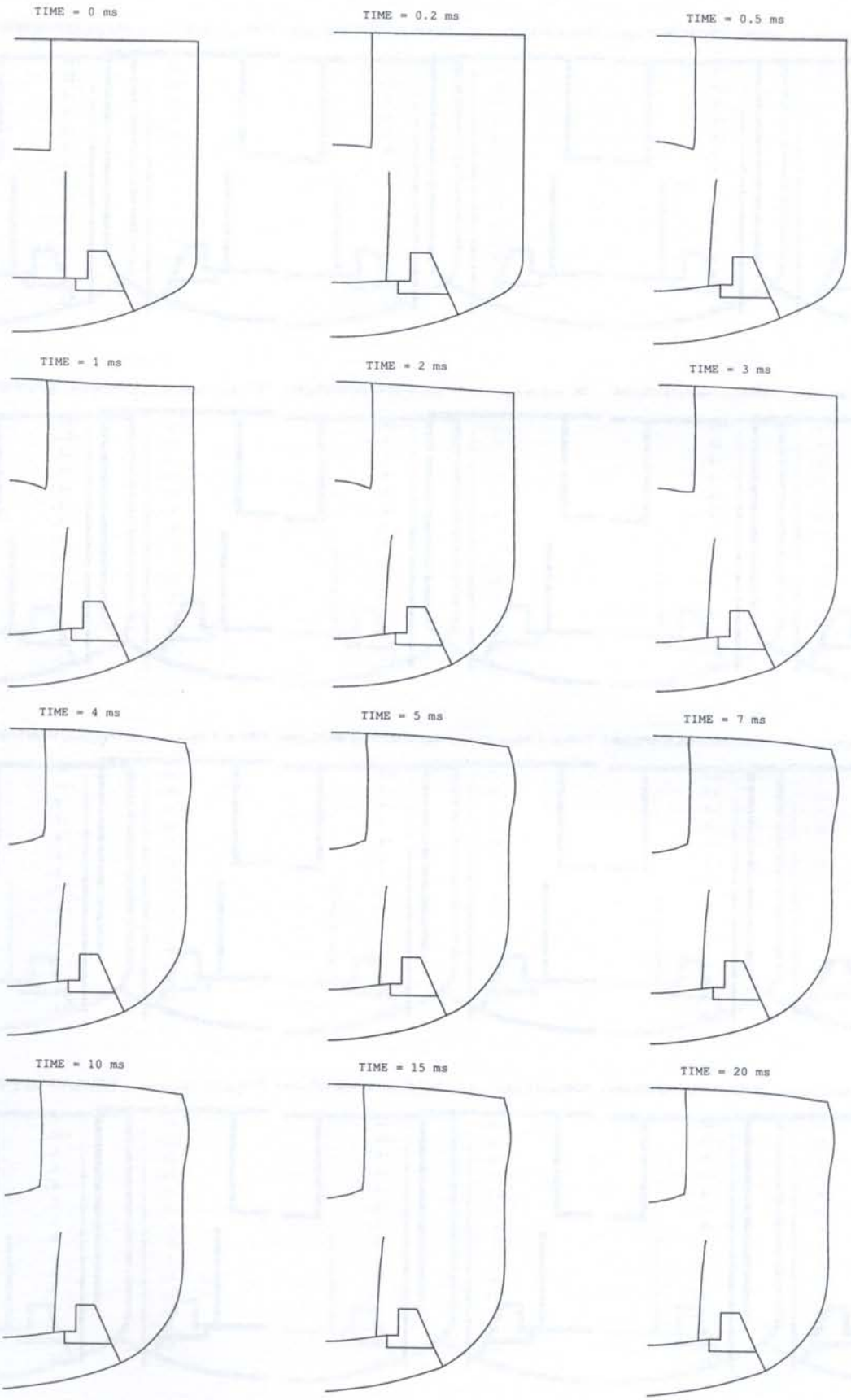

Fig. 14. Deformed shape of structures

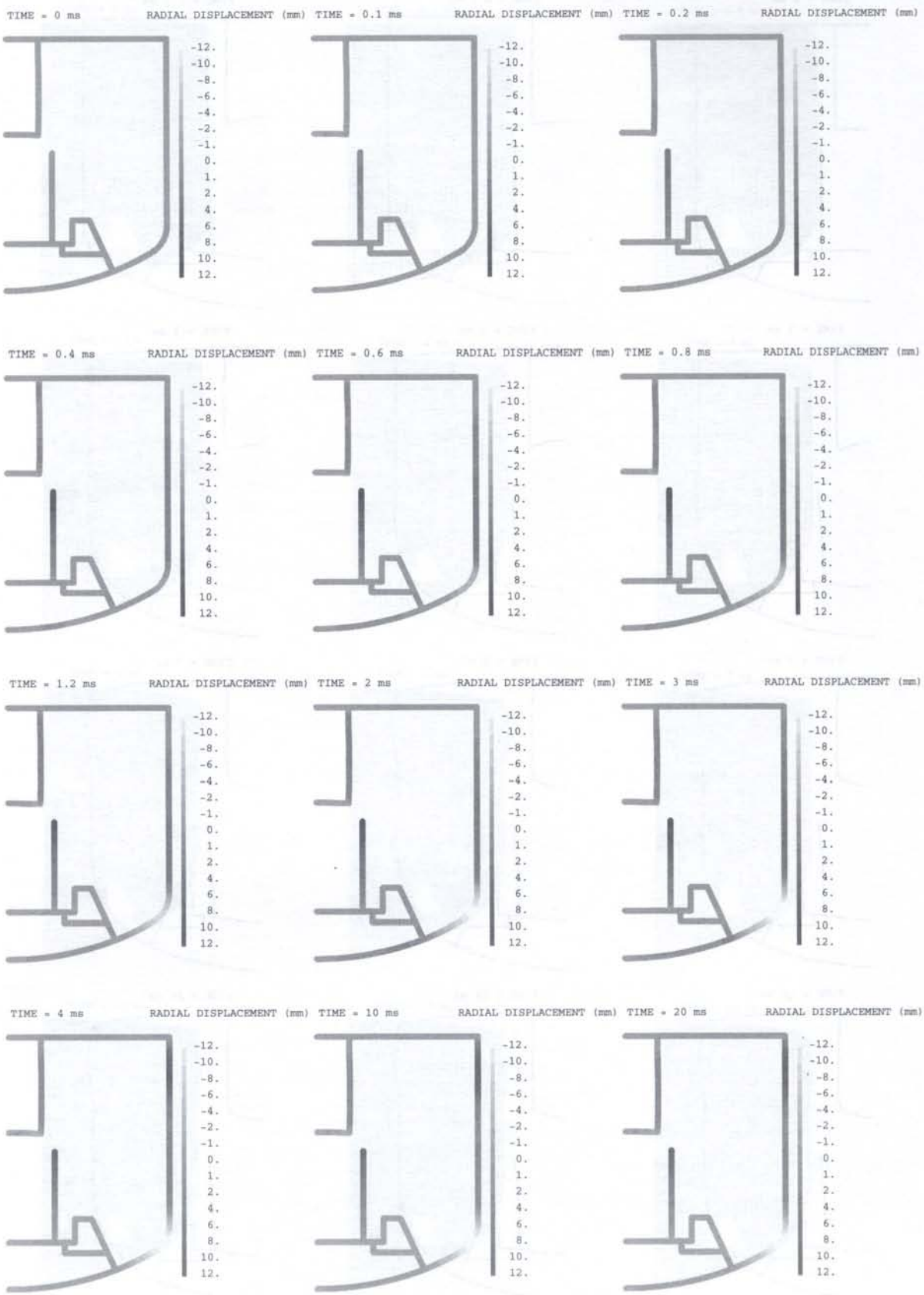

Fig. 15. Radial displacements of structures

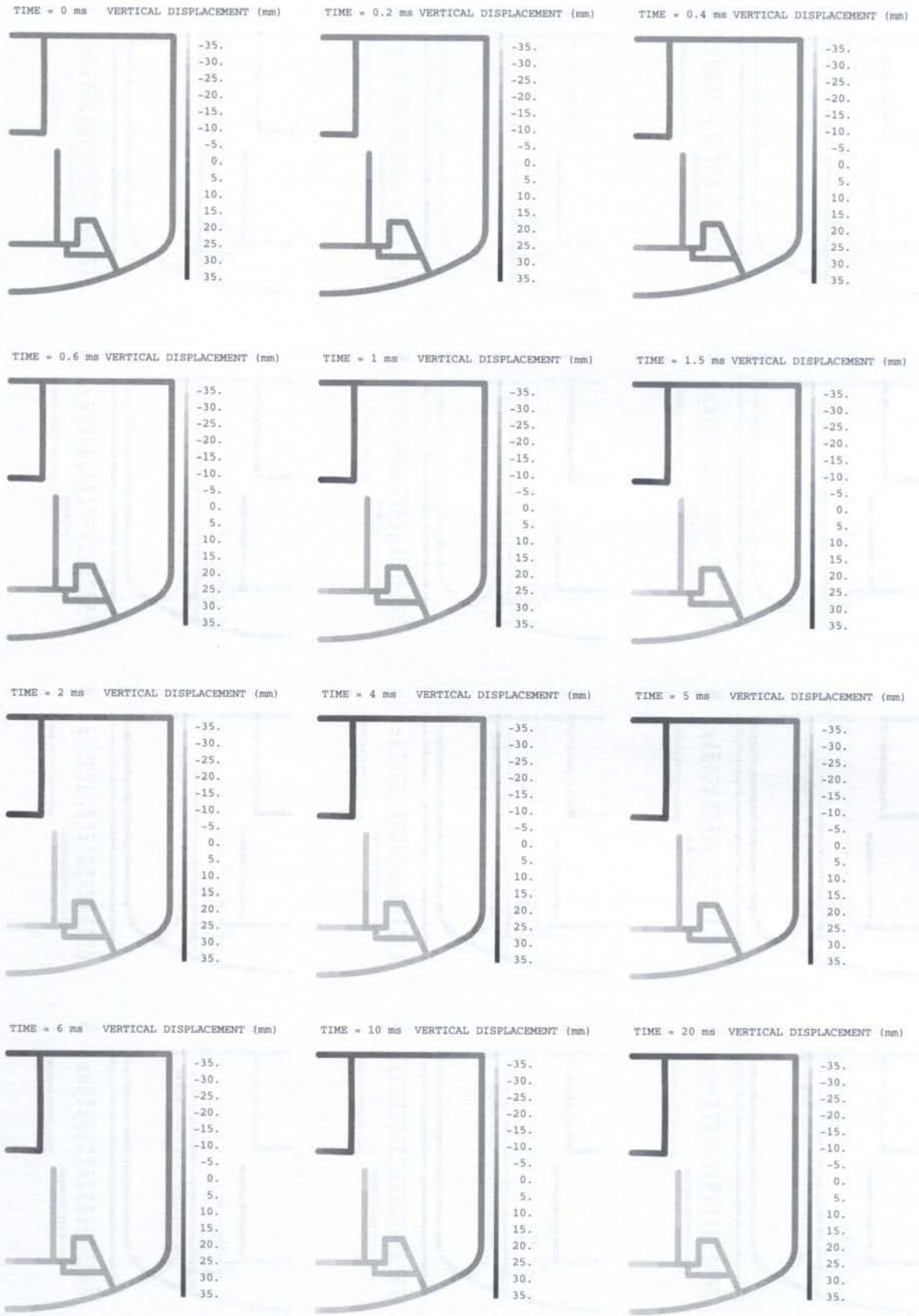

Fig. 16. Vertical displacements of structures

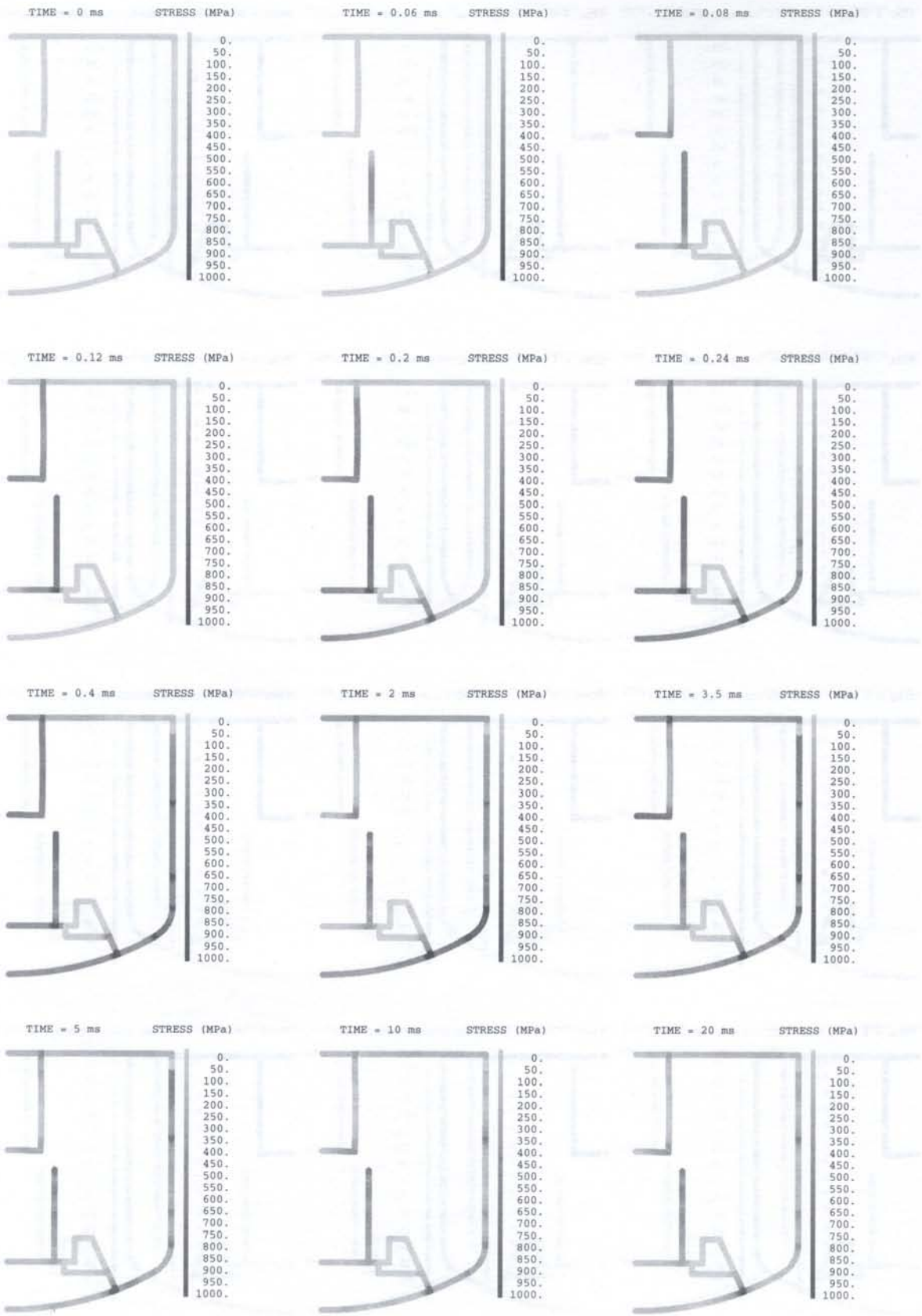

Fig. 17. Von Mises stresses

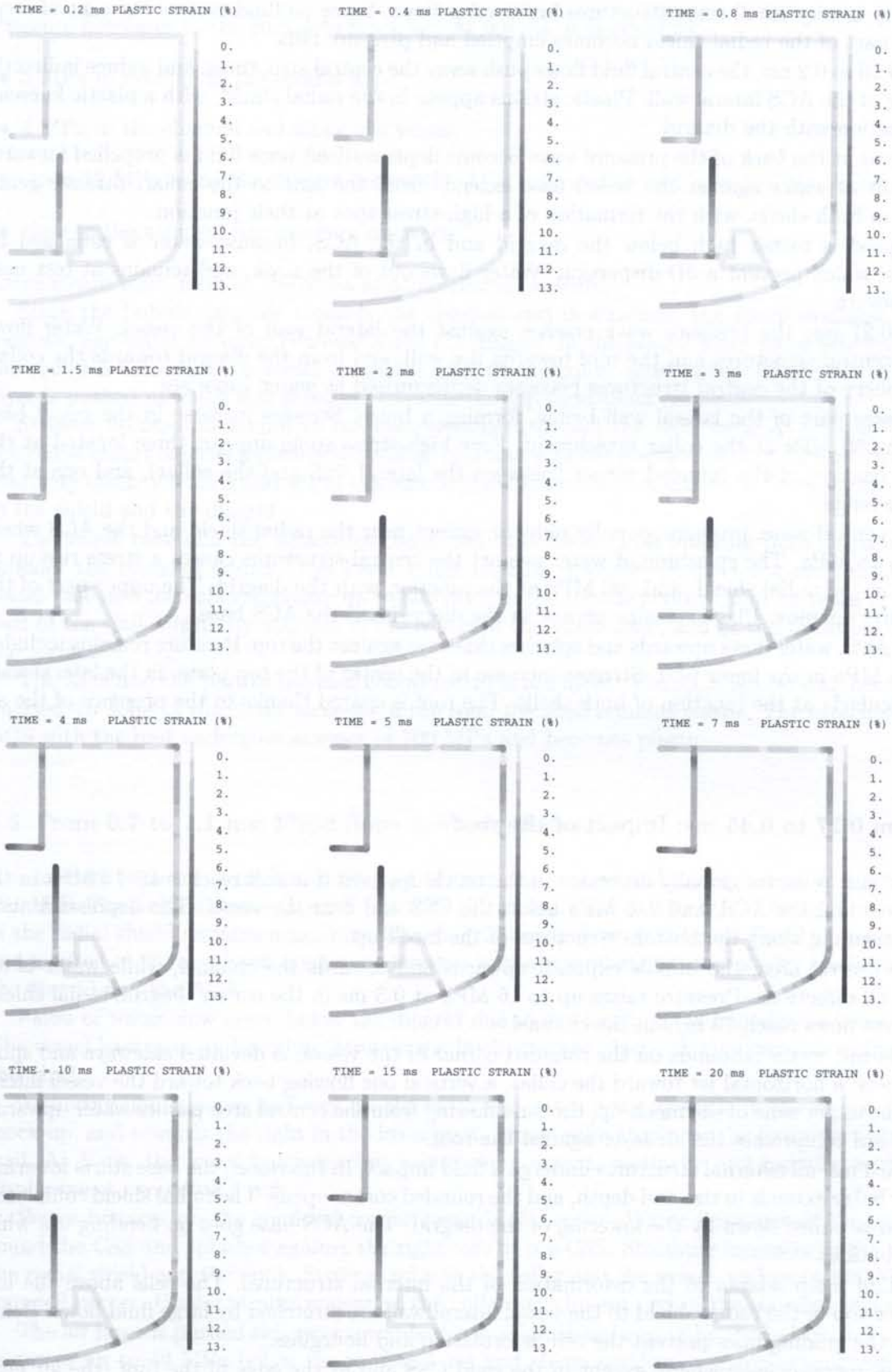

Fig. 18. Plastic strains

Pressure reaches 80 MPa at the bottom of the central area and in the nook. In both areas, the velocity is very small since structures limit water flows. Since no fluid crosses the central area, the outer part of the radial shield becomes emptied and pressure falls.

From 0.16 to 0.2 ms, the central fluid flows push away the central structures, and induce indirectly a buckling of the ACS lateral wall. Plastic strains appear in the radial shield, with a plastic kneecap at the junction with the diagrid.

The areas at the back of the pressure wave become depressurised since fluid is propelled forward. The impact of water against the vessel base extends from the axis to the collar. Stresses reach 350 MPa in both shells, with the formation of a high-stress spot at their junction.

The speed is rather high below the diagrid and in the ACS, because water is canalized by structures, which prevent a 3D-dispersion. Water flows out of the nook, and remains at rest near the top closure.

From 0.21 ms, the pressure wave crashes against the lateral wall of the vessel. Water flows from the central structures and the roof towards the wall, and from the diagrid towards the collar. The periphery of the central structures becomes depressurised as water vaporises.

The lower part of the lateral wall bends, forming a bulge. Stresses increase in the vessel base and reach 950 MPa at the collar attachment. Four high-stress spots appear: three located at the thickness changes of the rounded corner (between the lateral wall and the collar), and one at the top of the bulge.

In the central zone, pressure globally reduces, except near the radial shield and the ACS where it reaches 18 MPa. The splashing of water against the central structures causes a stress rise up to 650 MPa in the radial shield, and 900 MPa at the junction with the diagrid. The upper part of the shield starts opening. Plastic strains appear in the diagrid and the ACS base.

In the ACS, water flows upwards and splashes sideways against the top. Pressure remains included in 8 to 16 MPa in the lower part. Stresses increase in the centre of the top plate, in the lateral wall, and particularly at the junction of both shells. The roof is spared thanks to the presence of the air layer.

5.3. From 0.27 to 0.45 ms: Impact of the roof

From 0.27 ms, pressure globally decreases in the mock-up, even if it still reaches 10–14 MPa in the central area and the ACS, and 2–6 MPa below the CSS and near the vessel. The depressurisation induces steaming along the bottom structures of the mock-up.

In the central area, the bubble expands upwards and towards the channel, while water is expelled in all directions. Pressure raises up to 16 MPa at 0.3 ms in the corner diagrid/radial shield. The highest flows reach 70 m/s in the channel.

At 0.34 ms, water rebounds on the rounded corner of the vessel, is deviated sideways and splits into two jets: a horizontal jet toward the collar, a vertical one flowing back toward the vessel lateral wall. In the upper zone of the mock-up, the fluid flowing from the central area pushes water upwards, what in turn compresses the air layer against the roof.

From 0.4 ms, all external structures undergo a fluid impact. In the vessel, the base starts lowering, the lower bulge extends in size and depth, and the rounded corner opens. The radial shield completely opens and is pulled down by the lowering of the diagrid. The ACS base goes on bending up, while the wall buckles.

The fluid mesh adapts to the deformation of the internal structures. The cells above the line joining the top of the radial shield to the vessel lateral wall are stretched by large fluid flows. Below this line, the guiding lines prevent the cell deformation and hourglass.

Stresses increase everywhere, except in the rigid CSS and at the edge of the roof (the air layer protects the roof). The diagrid, the base and the lateral wall of the ACS become plastic. At the top of the radial shield, plastic strain reach 9%.

5.4. From 0.46 to 0.7 ms: Splash of fluid on the external structures

Pressure decreases in the complete mock-up. At 0.6 ms, it is equal to:

- 5 MPa in average in the central zone,
- 4 MPa in the channel and along the vessel,
- up to 12 MPa along the diagrid, below the ACS base and at mid-height of the ACS,
- close to the atmospheric pressure elsewhere.

Large steam trails form in the areas at atmospheric pressure.

Since the bubble expands towards the channel and downwards, the space available for water narrows, and water becomes confined along the diagrid. In the lateral zone, water rebounds against the rounded corner of the vessel to splash next to the collar attachment. Below the roof, the air layer is pushed upwards and sideways towards the top right-hand corner.

Stresses become maximum in the central structures and the ACS wall. At 0.6 ms, the top of the radial shield reaches a plasticity level of 13% and a radial displacement of 12 mm. Stresses and plasticity reach 500 MPa and 4% in the base and the lateral wall of the ACS. Then stresses diminish in the shield and the diagrid.

The vessel base and the structures connected to it lower. This lowering pulls down and makes rounder the rounded corner. The lower bulge extends upwards. Stresses remain constant in the vessel base and the collar, increase up to 800 MPa in the rounded corner, and decrease in the upper part of the wall. Plasticity appears in the centre of the vessel base, and at the thickness changes of the corner.

The ACS and the part of the roof connected to it are lifted. The ACS lateral wall becomes more buckled. In spite of the stress increase in the roof, the shell remains elastic. The attachment of the ACS with the roof undergoes stresses of 700 MPa and becomes plastic.

5.5. From 0.7 to 1.1 ms: Fluid flows towards the roof

The average pressure decreases down to 4 MPa in the central and lateral areas, and at the top of the ACS. The bubble starts expanding out of the central zone at 100 m/s. The opening at the top of the radial shield remains maximum. The diagrid bends down to 20 mm. The ACS base bends up and is lifted of 20 mm. Even if stresses decrease in the central structures, plastic strains increase in the diagrid and the ACS.

Flows of water slow down below the diagrid due to vaporisation, and accelerate below the CSS. The vessel base goes on lowering. Stresses diminish whereas plastic strains increase in the centre of this shell.

A sharing line appears half-way up the mock-up: water flows upwards in the upper part of the mock-up, and towards the right in the lower part. Flows quite stop near the lower part of the vessel wall. At 1 ms, the lower bulge reaches a maximum extent, vertically and radially, with a radial displacement exceeding 4 mm.

Water bounces on the rounded corner towards the collar. Water flows out of the nook, turns round the CSS and splashes against the right side of the CSS. Steaming increases in the vicinity of the radial shield and the nook. Stresses raise in the collar and the vessel, and reach 800 MPa in the rounded corner. Plastic strains appear at the collar attachment and in the rounded corner.

The air layer is pushed sideways towards the top right-hand corner by the bubble flows. Pressure increases up to 40 MPa below the roof at 1 ms and steam condenses. Stresses progressively raise from the centre to the edge of the roof, and in the upper part of the vessel lateral wall. The ACS lift pulls up the nearest part of the roof.

In the ACS, water is hurled against the top with a speed of about 20 m/s. The bottom is depressurised and water vaporises. The base bends, and the lateral wall buckles a bit more: a plastic strain level of 4% is recorded in both parts at 1 ms. The top undergoes stresses of 300 MPa and starts becoming plastic near the symmetry axis.

5.6. From 1.2 to 2 ms: Expansion of the bubble gas out of the central area

At 1.2 ms, the flow rate of the bubble crossing the channel increases in quantity and speed (up to 120 m/s), because the channel port becomes maximum: the radial shield is pulled down by the vessel base lowering while the ACS is pulled up by the roof lift.

Below the diagrid, water flows downwards and the steam bag expands until 1.5 ms. Then water flows back from the collar and the CSS towards the diagrid, pressurising again the area below the diagrid: steam condenses progressively. Velocities decrease down to 10 m/s.

From now onwards, the radial displacement of the radial shield remains equal to 12 mm. The centre of the diagrid and the vessel base lower down to 35 mm and 25 mm, respectively. In the ACS, the centre of the base and bottom right-hand corner are lifted up to 35 mm and 20 mm at 2 ms. Stresses decrease in the central structures, and evolve according to the orientation of the water flows in the vessel base.

In the nook, pressure decreases and water vaporises. The journey of the water flowing out of the nook shortens; fluid no longer impacts the outer side of the CSS but the top of the CSS. A whirlpool of steam appears at the top of the CSS.

Fluid flows slow down from the radial shield to the vessel lateral wall. A large steam layer forms along the radial shield. The lowering of the vessel base and the rounded corner goes on. Stresses remain stable in the corner and increase slightly in the lower part of the wall, whereas plastic strains increase in both parts of the vessel.

Above mid-height, water massively flows towards the roof, with relatively high velocities: between 10 and 50 m/s. A local pressurisation of 16 MPa at the two-third level of the mock-up appears since both bubble and water flows converge there. After 1.4 ms, pressure becomes lower than 3 MPa in the complete mock-up.

Below the roof, steam condenses and the air layer continues to be compressed and crushed. At 2 ms, the horizontal thrust of water towards the top right-hand corner simultaneously with the expansion of air from this corner leads to a concentration of air in a bag located at two-thirds of the radius.

In the ACS, the upwards water flows slow down progressively until becoming null. The ACS top is lifted of 20 mm at 2 ms, what pulls up the roof. Stresses decrease and plastic strain remain stable in the entire ACS. Stresses reach 300 MPa in the roof and the junction with the vessel becomes plastic.

5.7. From 2.1 to 3 ms: Massive flows towards the roof and slowing down in the lower part of the mock-up

In the central area, the bubble flows out with a speed up to 80 m/s, and the volume filled by the bubble remains stable. Below the diagrid, flows slow down and almost stop at 3 ms. The steam layer below the diagrid completely condenses. The collar hallmarks the vessel base and the global shape of the vessel is no longer regular.

Above the collar, the flows globally slow down and finally stop. The whirlpool of steam above the CSS expands vertically up to the top of the radial shield. The void fraction reaches approximately 60% in the nook, 80% along the radial shield, and 90% above the CSS at the bottom of the whirlpool. In the vessel rounded corner, stresses decrease while plastic strains increase.

The mesh is completely distorted in the nook due to the large upwards flows going out of this area. Between the shield and the vessel lateral wall, the mesh remains regular since the guiding lines limit the deformations.

The bubble largely expands above the top of the radial shield. The massive upwards water flows deviate towards the right from 2.5 ms. The highest speeds reach 120 m/s in the bubble panache and 30 m/s in water in direction of the top right-hand corner. Stresses decrease a little at 2.5 ms in the lateral wall of the vessel, but increase again at 3 ms.

The air layer is pushed horizontally towards the vessel, and transforms into a small bag flattened against the roof. The size of the bag becomes minimum at 3 ms. In the roof, after a slight decrease at 2.5 ms, stresses increase again at 3 ms, when the majority of the roof is lifted. The plastic kneecap in the top right-hand corner increases in size and plastic strains reach 3%.

In the ACS, water rebounds on the top and the lateral wall around 2.6 ms. The base bends down and comes back to a position close to the initial one. The bottom right-hand corner moves back sligthly to the right. Globally, the ACS starts coming back downwards. The lateral bulge persists because the up and down water flows impose a similar pressure against the wall.

In the ACS, stresses increase up to:

- 500 MPa in the bottom right-hand corner,
- 600 MPa in the top right-hand corner,
- 300 MPa in the upper part of the lateral wall and at the top.

The full ACS becomes plastic (plastic strains reach 5% in the upper part of the lateral wall), and a plastic kneecap forms at the junction with the roof.

5.8. From 3.1 to 4 ms: Formation of an upper bulge in the vessel

In the central area, the bubble fills three quarters of the space, and fluid mainly flows upwards, except below the ACS. Below the diagrid, water rebounds against the vessel base and water vaporises near the symmetry axis. The vessel base – and the structures linked to it – move back upwards and undergo less stresses.

Above the collar, water bounces back on the rounded corner and flows up. Water flows massively from the vessel lateral wall and splashes against the radial shield, what condenses the layer of steam. The whirlpool above the CSS is flattened progressively. Stresses greatly reduce in the vessel.

The size of the bubble panache is maximum at 4 ms. The panache expels water violently towards the roof and the top of the vessel. The upper part of the vessel deforms: stresses reach 550 MPa and the radial displacement 12 mm. Then fluid flows down along the wall; as the area of impact grows, the impact strength decreases.

Below the roof, the air bag expands back horizontally. Whereas water hits almost entirely the roof at 3.2 ms, water slides along the air bag and hits the roof only near the ACS at 4 ms. At that time, the roof suffers a maximum lift of 25 mm, stresses of 350 MPa, and becomes plastic (1%).

In the ACS, water alternates up and down flows according to the rebounds on the extremities of this cylinder. A steam layer forms alternately on the extremity emptied from water. The ACS base bends down from 3 ms onwards. Globally, the ACS is lifted and vertically stretched. At 3.5 ms, stresses increase up to 600 MPa in the centre of the ACS base and 850 MPa at the roof junction. Plastic strain reach 4% in the ACS lateral wall and 7% in the base.

5.9. From 4.1 to 6 ms: Stop of the panache expansion

In the central area, flows are oriented upwards. The bubble forms a thin jet between the centre of the area and the channel, and flows at a velocity included in 50 to 70 m/s. Stresses reach 650 MPa at the top of the radial shield.

Under the diagrid, flows slow down and a thin layer of steam covers the vessel base. The CSS and the diagrid are lifted, so the collar pulls up the vessel locally.

In the lateral area, flows from the vessel lateral wall accelerate and splash against the radial shield, forming two jets. Steam condenses along the radial shield. As fluid enters in the nook from 6 ms, the steam zone reduces but stays present there. Stresses decrease in the vessel base and the bottom of the lateral wall. The corner comes closer to the collar.

In the upper zone, fluid rebounds against the top closure, what stops the expansion of the bubble panache. Water goes round the bubble panache while the forefront is deviated and slides back on both sides of the panache. The outline of the panache becomes blurry because gas mixes with water.

The roof sligthly lowers back, and the air bag starts expanding downwards. The upper bulge at the top of the vessel reaches a maximum deformation at 6 ms. In spite of a global stress decrease in the roof and the upper part of the vessel, the plastic strains extend in the vessel.

In the ACS, water alternates rebounds against both extremities, with a decreasing velocity (< 10 m/s after 6 ms). Steam condenses at the top while water vaporises at the bottom. The ACS remains globally lifted, even if the centre of the base comes back to its initial location.

The bottom right-hand corner of the ACS rounds and the lateral wall buckles more. Stresses globally decrease in the plug, but still remain equal to 300 MPa in the rounded corner and the roof attachment. Plastic strains of 7% are observed in the centre of the ACS base, and in the buckled area.

5.10. From 6.1 to 8.5 ms: Formation of a whirlpool above the channel

The water going round the panache isolates the bubble gas in the panache from that in the central area. The gas starts twirling clockwise. The whirlpool sucks down fluid from the top of the mock-up.

Large flows of water slide down along the vessel lateral wall; they are deviated inwards before impacting the CSS and the radial shield. Flows are maximum at about 7.5 ms, then speed reduces. The steam in the nook is completely condensed from 7 ms on. Water vaporises slightly and temporarily at the right of the collar.

The whirlpool starts sucking up the bubble gas out of the central zone. But after 8 ms, it pushes it back into the central zone. Water is compressed against the diagrid. So the diagrid, radial shield, CSS and collar lower. In turn, the collar hallmarks down the vessel base locally.

The downward flows above the diagrid accelerate and propel the water below the diagrid towards the vessel base. The steam along the vessel condenses progressively. The fluid below the CSS bounces back, with an impact point that shifts towards the symmetry axis.

Stresses raise in the entire vessel and the collar. High-stress points appear at 8 ms, at the section changes of the vessel rounded corner, and at the limit between the lower bulge and the upper bulge. The vessel takes a pointed shape on the symmetry axis and undergoes plastic strains of 4%.

The air layer grows back downwards, especially from mid-roof to the top right-hand corner. Under the air layer, water flows down vertically near the vessel and horizontally towards the ACS. This latter flows accelerate so much that water shocks violently against the ACS attachment from 8 ms.

Water globally flows downwards in the ACS, except at the top. Water is vaporised at both extremities. Both roof and plug lower a little. Due to the unbalance between the flows on both faces of the ACS wall, the ACS lateral wall moves back inwards.

5.11. From 8.6 to 11 ms: Suction of water by the whirlpool and ejection of fluid in the central area

The bubble panache twirls round on its axis with a velocity included in 10 to 40 m/s. Centrifugation effects lead to a greatest concentration in gas in the outer part of the panache. As the gas mixes

with water at the periphery, the panache grows. The panache expels water towards the roof and the top of the vessel; then water slides down along the ACS and the vessel.

Water bounces back against the vessel, the CSS and the collar, and flows up massively. Water hits the rounded corner. Speeds reduce and almost stop in the vicinity of the CSS and the collar. Below the diagrid, water rebounds on the vessel base until 10 ms; then it deviates and hits the vessel under the CSS. For the second time, a steam layer forms above the vessel base.

The whirlpool sucks up and propels violently the water of the lateral area into the central area. Since the impact of water below the diagrid propels up the water at the bottom of the central area, the gas of this closed space becomes compressed at mid-height and fragments into several bags.

Below the roof, air flows countercurrent with respect to water until 9.5 ms: water flows towards the plug whereas air flows outwards. Later water concentrates around mid-roof. Even if a continuous layer of air covers the roof, air is mainly concentrated near the top right-hand corner.

In the ACS, water flows down and deviates towards the bottom left-hand corner until 10 ms, then towards the right one. A thin layer of steam covers both ends of the plug. The large flows entering in the central area lift a bit the ACS. The plug becomes the upper part of the mock-up and the top closure takes a more regular shape.

Stresses decrease in the vessel and the central structures, and remain stable in the upper ones. Apart a slight increase of the plastic strains in the centre of the vessel base, strains no longer evolve in the mock-up. Both vertical and horizontal displacements remain stable in the lower part of the mock-up, until the end of the simulation.

5.12. From 11.1 to 14 ms: Formation of a second whirlpool in the central area

The whirlpool goes on twirling and growing, but it expels water in all directions. Velocities reduce everywhere, and scarcely reach 40 m/s at the top of the panache and along the inner face of the radial shield.

Hurled by the whirlpool, fluid sweeps into the central zone, breaks up the bubble into three bags, and starts rotating inside this closed area. Even if this twirling flow strikes the radial shield, the shell does not move away any more.

Below the diagrid, water flows down and inwards. The impact point shifts towards the symmetry axis until 13 ms. Then water bounces back against the vessel, which condenses the steam layer. Stresses raise slightly at the point of impact, at the collar attachment and in the lateral wall.

Below the roof, air flows sideways towards the top right-hand corner. At about 13 ms, both water and air converge towards the corner and the volume of the air bag is very small. In the plug, water flows down in the centre and up along the lateral wall. However, flows become very weak.

5.13. From 14.1 to 17 ms: Ejection of fluid from the top right-hand corner

Both whirlpools twirl independently the one from the other. The panache has a maximum size, a shape close to a bowl and a maximum density in the middle. In the central area, the bubble is mainly confined on the left side of the diagrid. In the vicinity of the CSS and below the diagrid, water flows up at 14 ms, sideways at 16 ms and then downwards. A steam layer appears along the vessel base.

The air bag in the top right-hand corner expands down and ejects water far from the corner. Water divides into two jets: the one flows downwards along the lateral wall of the vessel and passes round the panache by the bottom, the other flows inwards and splashes against the top of the plug at 17 ms. The top of the ACS oscillates sligthly vertically. Stresses decrease in all structures.

5.14. From 17.1 to 20 ms: General slowing down of flows

Water rebounds a last time against the top of the ACS and the vessel base. Afterwards the fluid flows calm down everywhere. The air bag in the top right-hand corner grows spherically. The amplitude of both whirlpools reduces. The gas in the middle of the panache and above the diagrid expands and dilutes among water. The velocity becomes slower than 30 m/s in both whirlpools. In spite of this lull, stresses raise at different locations of the vessel.

5.15. Comparison with the experimental results

Table 1 presents the comparison of the current results computed by Europlexus, with the experimental results of the MARA 10 test. Globally, the EUROPLEXUS simulation is in good agreement with experimental results, apart from the deformation of the radial shield, the ACS and the upper bulge.

Table 1. Comparison between the experimental and numerical results

		Experiment		EP computations	
		Maximum	Final	Maximum	Final
Vessel bottom	Vertical displacement (cm)	3.8	2.7	3.05	2.8
Vessel lower bulge	Hoop strain (%)	1.7	1.3	1.4	1.2
Vessel upper bulge	Hoop strain (%)	2.9	2.7	4.1	3.8
	Distance to the roof (cm)		6.3		7.6
Roof	Vert. displacement in the centre (cm)	3.1	1.9	2.8	2.25
	Vert. displacement at mid-radius (cm)	2.0	1.4	2.0	1.8
	Instant of max (ms)	3.8		4.5	
Diagrid	Vert. displacement in the centre (cm)		3.1	3.75	3.2
Radial shield	Hoop strain (%)	6.0	4.2	13	12.6
Lateral wall of the ACS	Hoop strain of the bulge (%)		6.4	3.1	2.9
	Vertical strain of the wall (%)		−2.6		−1.7
Base of the ACS	Vertical displacement (cm)			3.3	0.6
	Height increase on axis (%)	2.4		7.6	
		1st impact	2nd impact	1st impact	2nd impact
Pressure under the roof	Maximum pressure (MPa)	25	9	centre: 19 else: 15	centre: 14 else: 9
	Instant of the maximum (ms)	0.5	4.5 to 5.5	0.25	4 to 5.5

The gaps between the experimental results and the deformations predicted for the vessel bottom, the lower bulge of the vessel lateral wall, the diagrid and the roof, are lower than 20%. For the bulges at the top of the vessel wall and in the ACS lateral wall, the gap is included in 35 to 55%. The prediction of the radial shield opening and the ACS lift is really overestimated with 100 to 200% error.

The radial shield deforms with a moon shape in the test whereas it opens like a flower in the simulation. The ACS cylindrical wall presents two bulges in the test, whereas only the lower one forms in the simulation. These discrepancies may take their origin into the simplifications adopted

in the numerical model: the pinned attachment at the base of the radial shield was not modeled, nor the stiffening of the corner between the ACS base and the ACS wall.

The comparison of the EUROPLEXUS results with the experimental results, and with previous results computed with the codes SIRIUS and CASTEM-PLEXUS is described more in detail in [56].

6. Conclusion

This paper is divided into a theoretical part describing the numerical models of the EUROPLEXUS code, and an application to the simulation of a Hypothetical Core Disruptive Accident in the MARA 10 mock-up. EUROPLEXUS is a general fast dynamics code for fluids and solids, with a possible coupling. The algorithm and equations of the code are presented for the Arbitrary Lagrange Euler description, as well as the methods used to treat the fluid-structure interaction. The CDA constitutive law, implemented in the EUROPLEXUS code on purpose for computing this kind of explosion, is described in detail.

The MARA 10 mock-up represents a simplified geometry of a Liquid Metal Fast Breeder Reactor. The fluids intervening in the real accident are replaced by water, air and an explosive charge in the experiment. In the numerical model, fluids are described by the specific CDA constitutive law, and structures by elastic-plastic shells. The EUROPLEXUS code succeeds in carrying out the computation of the explosion for 20 ms of physical time.

The explosive charge in the centre causes the propagation of a pressure wave that impacts first the internal structures and then the containment. The bubble gas expands in the central zone confined by the internal structures. Then it flows out in the rest of the mock-up by the outlet between the ACS and the radial shield. Water vaporises around the radial shield, below the diagrid and in the ACS. The air layer is compressed under the roof by the water thrown upwards by the explosion.

Very soon, the diagrid moves down, the radial shield moves away and the ACS base moves up. Then the vessel base lowers and the lateral wall goes away, creating a lower bulge. The ACS lateral wall buckles, the ACS top is lifted, thus pulling up the rest of the roof. Finally, an upper bulge creates in the upper part of the lateral wall of the vessel and the ACS base changes curvature.

The numerical results are globally in good agreement with the experimental ones, apart from the prediction of the deformation of the ACS, the radial shield and the upper bulge of the vessel lateral wall.

In the future, the results may be improved by using constitutive laws closer to the materials, in particular for the vessel. All structures were modeled with isotropic Von Mises laws, using experimental strain-stress curves given by static and dynamic tensile tests.

The material behaviour depends on both the strain rate during the test, and – for the vessel – the initial hardening induced by the cold work. Both parameters were considered by dividing the vessel into four zones corresponding to an average hardening and a given strain rate. An adaptation of the constitutive law to the evolution of the strain rate versus time should improve the numerical predictions concerning the vessel.

References

[1] D. Acker, A. Benuzzi, A. Yerkess, J. Louvet. MARA 01/02 – Experimental validation of the SEURBNUK and SIRIUS containment codes. *Proc. 6th Int. Conf. on Structural Mechanics In Reactor Technology*, paper E 3/6. Paris, France, 1981.

[2] C. Albertini, et al. The JRC-COVA programme: Final Report. Commission of the European Communities, Report EUR 8705. *Nuclear Science and Technology*, 1–182, 1984.

[3] A. Benuzzi. Comparison of different LMFBR primary containment codes applied to a benchmark problem. *Nuclear Engineering and Design*, **100**: 239–249, 1987.

[4] Y. Blanchet, P. Obry, J. Louvet. Treatment of fluid-structure interaction with the SIRIUS computer code. *Proc. 6th Int. Conf. on Structural Mechanics In Reactor Technology*, paper B 8/8. Paris, France, 1981.

[5] C. Bour, M. Spérandio, J. Louvet, C. Rieg. LMFBR's core disruptive accident. Mechanical study of the reactor block. *Proc. 10th Int. Conf. on Structural Mechanics In Reactor Technology*, Vol. E, 281–287. Anaheim, USA, August 1989.

[6] H. Bung, F. Casadei, J.P. Halleux, M. Lepareux. PLEXIS-3C: A computer code for fast dynamic problems for structures and fluids. *Proc. 10th Int. Conf. on Structural Mechanics In Reactor Technology*, Vol. B, 85-90. Anaheim, USA, August 1989.

[7] D.J. Cagliostro, A.L. Florence, G.R. Abrahamson. Scale modeling in LMFBR safety. *Nuclear Engineering and Design*, **55**: 235–247, 1979.

[8] I.G. Cameron, B.C. Hankin, A.G.P. Warham, A. Benuzzi, A. Yerkess. The computer code SEURBNUK-2 for fast reactor explosion containment safety studies. *Proc. 4th Int. Conf. on Structural Mechanics In Reactor Technology*, paper B 2/1. San Francisco, USA, 1977.

[9] Y. Cariou, M. Spérandio, M. Lepareux, K. Christodoulou. LMFBR's whole core accident. Validation of the PLEXUS code by comparison with MARA tests. *Proc. 12th Int. Conf. on Structural Mechanics In Reactor Technology*, paper E 7/4. Stuttgart, Germany, August 1993.

[10] Y. Cariou, J.P. Pirus, C. Avallet. LMR large accident analysis method. *Proc. 14th Int. Conf. on Structural Mechanics In Reactor Technology*, paper P 3/7, 395–402, Lyon, France, August 1997.

[11] F. Cadadei, A. Daneri, G. Toselli. Use of PLEXUS as a LMFBR primary containment code for the CONT benchmark problem. *Proc. 10th Int. Conf. on Structural Mechanics In Reactor Technology*, paper E 13/1, 299–304. Anaheim, USA, August 1989.

[12] F. Casadei, J.P. Halleux. An algorithm for permanent fluid-structure interaction in explicit transient dynamics. *Computer Methods in Applied Mechanics Engineering*, **128** (3-4): 231–289, 1995.

[13] F. Casadei. Recent advances in the modelling of fast transient fluid-structure interactions of the permanent type. *Proc. 14th Int. Conf. on Structural Mechanics In Reactor Technology*, paper B 07/1. Lyon, France, August 1997.

[14] F. Casadei, J.P. Halleux, A. Sala, F. Chillè. Transient fluid-structure interaction algorithms for large industrial applications. *Computer Methods in Applied Mechanics Engineering*, **190** (24-25): 3081–3110, 2001.

[15] F. Casadei. Algorithms for fast transient fluid-structure interactions, *Proc. User Conference SAMTECH*. Paris, France, January 2001.

[16] F. Casadei, J.P. Halleux. Europlexus: A numerical tool for fast transient dynamics with fluid-structure interaction. *Proc. SAMTECH users conference*. Toulouse, France, February 2003.

[17] Y.W. Chang, J. Gvildys, S.H. Fistedis. Analysis of the primary containment response using a hydrodynamic-elastic-plastic computer code. *Nuclear Engineering and Design*, **27**: 155–175, 1974.

[18] Y.W. Chang. Application of containment codes to LMFBRs in the United States. *Nuclear Engineering and Design*, **42**: 53-67, 1977.

[19] C. Chavant, A. Hoffmann, P. Verpeaux, J. Dubois. Plexus: A general computer code for explicit Lagrangian computation. *Proc. 5th Int. Conf. on Structural Mechanics In Reactor Technology*, paper B 2/8. Berlin, Germany, 1979.

[20] M. Cigarini, A. Daneri, G. Toselli. Applications of ASTARTE-4 code to explosive models with complex internal structure using the rezoning facility. *Proc. 7th Int. Conf. on Structural Mechanics In Reactor Technology*, paper B 9/3. Chicago, USA, 1983.

[21] M.S. Cowler, S.L. Hancock. Dynamic fluid-structure analysis of shells using the PISCES 2 DELK computer code. *Proc. 5th Int. Conf. on Structural Mechanics In Reactor Technology*, paper B 1/6. Berlin, Germany, 1979.

[22] A. Daneri, G. Toselli, T. Trombetti, Y. Blanchet, J. Louvet, P. Obry. Influence of the representation models of the stress-strain law on the LMFBR structures in an HCDA. *Proc. 6th Int. Conf. on Structural Mechanics In Reactor Technology*, paper E 4/4. Paris, France, 1981.

[23] F. David. Etude d'une composition explosive flegmatisée. Applications à la déformation d'une cuve. *Proc. Symposium sur les hautes pressions dynamiques*. Paris, France, 1978.

[24] J. Donéa, A. Huerta, F. Casadei. Finite element models for transient dynamic fluid-structure interaction. *New advances in Computational Structural Mechanics*: 335–346, 1992.

[25] M. Falgayrettes, C. Fiche, P. Granet, P. Hamon, P. Barrau, B. Magnon, J. Jalouneix, M. Nédélec. Response of a 1/20-scale mock-up of the Superphenix breeder reactor to an HCDA loading simulation. *Proc. 7th Int. Conf. on Structural Mechanics In Reactor Technology*, paper E 4/1, 157–166. Chicago, USA, 1983.

[26] C. Fiche, J. Louvet, B.L. Smith, A. Zucchini. Theoretical experimental study of flexible roof effects in an HCDA's simulation. *Proc. 8th Int. Conf. on Structural Mechanics In Reactor Technology*, paper E 4/5, 139–144. Brussels, Belgium, 1985.

[27] S. Giuliani. An algorithm for continuous rezoning of the hydrodynamic grid in Arbitrary Lagrangian Eulerian codes. *Nuclear Engineering and Design*, **72**: 205–212, 1982.

[28] J.L. Graveleau, P. Louvet. Calculation of fluid-structure interaction for reactor safety with the CASSIOPEE code, *Proc. 5th Int. Conf. on Structural Mechanics In Reactor Technology*, paper B 1/7. Berlin, Germany, 1979.

[29] L. Haar, J.S. Gallagher, G.S. Kell. NBS/NRC Steam tables. In: *Hemisphere Publishing Corporation*, Taylor & Francis Group, Bristol, 1984.

[30] A. Hoffmann, M. Lepareux, B. Schwab, H. Bung. Plexus – A general computer program for fast dynamic analysis. *Proc. Conference on Structural Analysis and Design on Nuclear Power Plant.* Porto Alegre, Brazil, 1984.

[31] H. Holtbecker. Testing philosophy and simulation techniques. *Nuclear Engineering and Design*, **42**: 75–87, 1977.

[32] N. E. Hoskin, M. J. Lancefield. The COVA programme for the validation of computer codes for fast reactor containment studies. *Nuclear Engineering and Design*, **46**: 17–46, 1978.

[33] K. C. Kendall, A. Benuzzi. The COVA programme: Validation of the fast reactor containment code SEURBNUK. *Nuclear Engineering and Design*, **57**: 79–105, 1980.

[34] K. C. Kendall, D. J. Adnams. Experiments to validate structural dynamics code used in fast reactor safety assessment. In: Science and Technology of Fast Reactor Safety, Vol. 2, *British Nuclear Energy Society.* London, England, 1986.

[35] M. Lepareux, B. Schwab, H. Bung. Plexus: A general computer program for the fast dynamic analysis. The case of pipe-circuits. *Proc. 8th Int. Conf. on Structural Mechanics In Reactor Technology*, paper F1 2/1. Brussels, Belgium, 1985.

[36] M. Lepareux, A. De Gayffier, H. Bung, A. Letellier. Réflexions sur les méthodes de la dynamique explicite dans Castem2000 et Plexus (in French). CEA report DMT/96-473, 1996.

[37] M. Lepareux, H. Bung, A. Combescure, J. Aguilar. Analysis of a CDA in a LMFBR with a multiphasic and multicomponent behaviour law. *Proc. 11th Int. Conf. on Structural Mechanics In Reactor Technology*, paper E 13/1, 371–376. Tokyo, Japan, August 1991.

[38] M. Lepareux, H. Bung, A. Combescure, J. Aguilar, J. F. Flobert. Analysis of an HCDA in a fast reactor with a multiphase and multicomponent behavior law. *Proc. 12th Int. Conf. on Structural Mechanics In Reactor Technology*, paper E 7/2, 197–202. Stuttgart, Germany, August 1993.

[39] M. Lepareux, J. M. Michelin, D. Thiault. Plexus-R: une extension de Plexus à la robotique (in French). CEA report DMT/94-138, 1994.

[40] J. Louvet, P. Hamon, B. L. Smith, A. Zucchini. MARA 10: an integral model experiment in support of LMFBR containment analysis. *Proc. 9th Int. Conf. on Structural Mechanics In Reactor Technology*, Vol. E, 331–337. Lausanne, Switzerland, 1987.

[41] J. Louvet. Containment response to a core energy release. Main experimental and theorical issues - Future trends. *Proc. 10th Int. Conf. on Structural Mechanics In Reactor Technology*, Vol. E, 305–310. Anaheim, USA, 1989.

[42] NERSA. The Creys-Malville power plant. In: *Electricité de France*, Direction de l'équipement, Région d'équipement Alpes-Lyon, France, 1987.

[43] S. Potapov, F. Bliard, F. Tephany. Simulation de la décompression du réacteur HDR avec le code de dynamique rapide EUROPLEXUS. *Revue Européenne des Eléments Finis*, **11**(5): 667–694, 2002.

[44] S. Potapov. Modelling of Aquitaine II pipe whipping test with Europlexus fast dynamic code. *Proc. 17th Int. Conf. on Structural Mechanics In Reactor Technology*, paper P 01/5. Prague, Czechoslovakia, August 2003.

[45] M. F. Robbe, M. Lepareux, H. Bung. Plexus – Notice théorique. CEA report DMT/94-490, 1994.

[46] M. F. Robbe, N. Vivien, M. Valette, E. Berglas. Use of thermalhydraulic and mechanical linked computations to estimate the mechanical consequences of a steam explosion. *Journal of Mechanical Engineering*, **52**(2): 65–90, 2001.

[47] M. F. Robbe, M. Lepareux, E. Treille, Y. Cariou. Numerical simulation of an explosion in a simple scale model of a nuclear reactor. *Journal of Computer Assisted Mechanics and Engineering Sciences*, **9**(4): 489–517, 2002.

[48] M. F. Robbe, M. Lepareux. Evaluation of the mechanical consequences of a steam explosion in a nuclear reactor. *Bulgarian Journal of Theoretical and Applied Mechanics*, **32**(1): 48–84, 2002.

[49] M. F. Robbe, F. Bliard. A porosity method to describe the influence of internal structures on a fluid flow in case of fast dynamics problems. *Nuclear Engineering and Design*, **215**: 217–242, 2002.

[50] M. F. Robbe, M. Lepareux, C. Trollat. Hydrodynamic loads on a PWR primary circuit due to a LOCA. *Nuclear Engineering and Design*, **211**: 189–228, 2002.

[51] M. F. Robbe, M. Lepareux, Y. Cariou. Numerical interpretation of the MARA 8 experiment simulating a Hypothetical Core Disruptive Accident. *Nuclear Engineering and Design*, **220**: 119–158, 2003.

[52] M. F. Robbe, M. Lepareux, E. Treille, Y. Cariou. Numerical simulation of a Hypothetical Core Disruptive Accident in a simple scale model of a nuclear reactor. *Nuclear Engineering and Design*, **223**(2): 159–196, 2003.

[53] M. F. Robbe, P. Sardain. Comparison of several simplified models and scenarios to simulate a steam explosion in a tank. *Journal of Mechanical Engineering*, **54**(2): 82–100, 2003.

[54] M. F. Robbe, S. Potapov. Modeling of the depressurisation induced by a pipe rupture in the primary circuit of a nuclear plant. *Revue Européenne des Eléments Finis*, **12**(4): 459–485, 2003.

[55] M. F. Robbe, S. Potapov, F. Teffany. Simulation of the depressurisation occuring at the beginning of a LOCA in a 4-loop PWR. *Nuclear Engineering and Design*, **224**: 33–63, 2003.

[56] M. F. Robbe, F. Casadei. Comparison of different models to simulate a Core Disruptive Accident in the MARA 10 mock-up. *Nuclear Engineering and Design*, **232**: 301–326, 2004.

[57] J. E. A. Sidoli, K. C. Kendall. The WINCON programme – Validation of the fast reactor primary containment codes, *Proc. INE Int. Conf. On Nuclear Containment*, Cambridge, England, April 1987. In: *Nuclear Containment Structures*, D. G. Walton, ed., Cambridge University Press, 1988.

[58] B. L. Smith, A. Yerkess, J. Adamson. Status of coupled fluid-structure dynamics code SEURBNUK. *Proc. 7th Int. Conf. on Structural Mechanics In Reactor Technology*, paper B 9/1. Chicago, USA, 1983.

[59] B. L. Smith, C. Fiche, J. Louvet, A. Zucchini. A code comparison exercise based on the LMFBR containment experiment MARA-04. *Proc. 8th Int. Conf. on Structural Mechanics In Reactor Technology*, paper E 4/7, 151–157. Brussels, Belgium, 1985.

[60] B. L. Smith, A. Yerkess, V. Washby. The computer code SEURBNUK-EURDYN: First release version. *Proc. 9th Int. Conf. on Structural Mechanics In Reactor Technology*. Lausanne, Switzerland, 1987.

[61] M. Stiévenart, P. Bouffioux, M. Eglème, J. P. Fabry, H. Lamotte. Analysis of LMFBR explosion model experiments by means of the Surboum-II code. *Proc. 3rd Int. Conf. on Structural Mechanics In Reactor Technology*, paper E 3/5. London, England, 1975.

[62] E. Studer, P. Galon. Hydrogen combustion loads – Plexus calculations. *Nuclear Engineering and Design*, **174**: 119–134, 1997.

[63] H. U. Wenger, B. L. Smith. On the origin of the discrepancies between theory and experiment in the COVA series. *Proc. 9th Int. Conf. on Structural Mechanics In Reactor Technology*, Vol. E, 339–344. Lausanne, Switzerland, 1987.

[64] P. H. West, N. E. Hoskin. APRICOT – Phase 3. Suggested simple test problems for examination of thin shell modelling and fluid structure coupling. Aldermaston report AWRE/44/92/16, 1980.